DETERMINATION OF THE MIXED MODE STRESS INTENSITY FACTOR ON WEAKENED PLANES FOR CENTRALLY CRACKED POLYCARBONATE

By

KYLE R. MESSER
Bachelor of Mechanical Engineering
University of Tulsa
Tulsa, OK
2019

Submitted to the Faculty of the
Graduate College of
Oklahoma State University
in partial fulfillment of
the requirements for
the Degree of
MASTER OF SCIENCE
DECEMBER, 2022

DETERMINATION OF THE MIXED MODE STRESS INTENSITY FACTOR ON WEAKENED PLANES FOR CENTRALLY CRACKED POLYCARBONATE

Thesis Approved:

Raman Singh

Jake Bair

Ranji Vaidyanathan

ACKNOWLEDGMENTS

I would like to thank Dr. Raman Singh, my advisor, who guided me through my graduate school experience and allowed me to participate in research that provided me with the knowledge that I would not receive anywhere else.

Additionally, I would like to thank our lab's postdoc, Ali Fahem, whose optimism brought a positive atmosphere that would not be achieved by anybody else. His devotion and knowledge in the lab have allowed for research progress that otherwise would not have been possible.

To the OSU community, including my lab partners and friends, I would like to say thank you for the memories and good times we had on campus together. You turned my graduate school times into a phenomenal experience. I hope to keep these friendships as we move forward in life.

To my committee members, Dr. Ranji Vaidyanathan and Dr. Jake Bair, thank you for helping guide me through this experience.

I would like to acknowledge the Department of Energy for the financial support in funding this research.

Acknowledgments reflect the views of the author and are not endorsed by committee members or Oklahoma State University.

DEDICATION

I would like to dedicate this thesis to three of the most important people in my life; my mother, my father, and my wife.

I would like to thank my parents for their constant support of my education and life goals. They inspired me to achieve more through education, and their encouragement was critical to my success in graduate school and to shaping who I am today.

To my wife, Anahi Messer, your support has carried us through many challenges. Your help in continuing my education has made the difficult times seem enjoyable. I could never hope to achieve this goal without the constant love and encouragement that you have continuously given me throughout these years. I look forward to the memories we will make together.

Acknowledgments reflect the views of the author and are not endorsed by committee members or Oklahoma State University.

Name: KYLE R. MESSER

Date of Degree: DECEMBER, 2022

Title of Study: DETERMINATION OF THE MIXED MODE STRESS INTENSITY FACTOR ON WEAKENED PLANES FOR CENTRALLY CRACKED POLYCARBONATE

Major Field: MATERIALS SCIENCE AND ENGINEERING

Abstract: The dynamic behavior of materials has been of interest for over a century. The development of high impact technology has seen great interest recently with notable fields such as weaponry, aerospace, automotive, and geoscience. There is a significant need to understand high impact on weakened plane materials. This need has greatly increased due to the advances in both manufacturing and geotechnical material response. On the manufacturing side, advances in 3D printing has lead to greater use and a broader application base. However, weakened planes are formed when subsequent layering of old and new layers are placed. Additionally, composite materials have a inherent weakened planes between fiber and matrix. On the geotechnical side, shale is critical in the extraction of oil and natural gas. In order to extract petroleum, shale must be broken to allow flow which is complicated by foliation. The influences of this fracture can be attributed to stress wave interactions across the weakened planes. However, in spite of its many applications, stress wave interactions along weakened planes has not been fully explained. This research aims to explain mixed mode fracture interactions along weakened planes by means of stress wave propagation. This is achieved by the use of a rectangular specimen that is through cut and glued back together with a central starter crack left to initiate fracture caused by a split-Hopkinson pressure bar (SHPB) and recorded using two high speed cameras. Digital Image Correlation (DIC) is used to measure both farfield, and nearfield crack tip opening displacement (CTOD) data while strain gauges on a SHPB use voltage generated from the pulse wave, is utilized to gain fracture toughness values. The stress wave propagation is broken into elastic, shear, and fracture regions and a fracture envelope is created for angles of 15° 30°, 45° and 60°. A 75° angle was attempted but was outside of the fracture envelope.

TABLE OF CONTENTS

Chapter Page

I Introduction **1**
1.1 The dynamic behavior of materials 1
1.2 Stress wave interactions and strain rates 7
1.3 Mixed mode fracture interactions 9
1.4 Stress wave response in the presence of cracked bodies 10
1.5 Crack tip opening displacement and plastic zone 11

II Experimental Setup **13**
2.1 Components of the experimental apparatus 13
2.2 Brief history of the split-Hopkinson pressure bar 16
2.3 Brief history of digital image correlation 18

III Methods **20**
3.1 Specimen preparation 20
3.2 Assumptions and sources of error 23
3.3 Theory of equations for the split Hopkinson pressure bar 24
3.4 Theory of equations for digital image correlation 25
3.5 Results 27
3.6 The 15 degree results 28
3.7 The 30 degree results 37
3.8 The 45 degree results 46
3.9 The 60 degree results 55
3.10 The 75 degree results 64
3.11 Fracture envelope and summary of results 65

IV Conclusion **67**

V Future work **69**

References **69**

A Geometry Factor Deviation **77**

LIST OF TABLES

Table Page

3.1 Material properties of cyanoacrylate 21

3.2 Polycarbonate along centrally cracked weakened planes dynamic fracture toughness for a weakened plane angle of 15° 37

3.3 Polycarbonate along centrally cracked weakened planes dynamic fracture toughness for a weakened plane angle of 30° 46

3.4 Polycarbonate along centrally cracked cyanoacrylate weakened planes dynamic fracture toughness for a weakened plane angle of 45° 55

3.5 Polycarbonate along centrally cracked weakened planes dynamic fracture toughness for a weakened plane angle of 60° 64

3.6 Cyanoacrylate weakened planes on bulk polycarbonate showing fracture toughness average and standard deviation of each angle for nearfield view 66

LIST OF FIGURES

Figure Page

1.1 Number bar showing the effects strain rates for different loading conditions 8
1.2 The three modes of fracture with directional loading 10
1.3 Force lines though a block 11
1.4 Crack tip and path showing 45° lines with plastic zone 12

2.1 Not to scale split Hopkinson pressure bar testing schematic . . . 13
2.2 Not to scale digital image correlation and camera testing schematic 13
2.3 Farfield image of a 60 degree test 15
2.4 Nearfield image of a 60 degree test 15
2.5 Movement of nearfield speckle on specimen captured by DIC . . 16
2.6 Timeline of the development of split Hopkinson pressure bar . . 17

3.1 Cut specimen 22
3.2 Corner view of taped specimen 22
3.3 Specimen glued with starter crack 22
3.4 White base on specimen 22
3.5 Farfield specimen 22
3.6 Nearfield specimen 22
3.7 Free body diagram on a triangular surface at an angle 25
3.8 Split Hopkinson pressure bar raw values of test 1 with vertical lines indicating transfer of stress waves 29

Figure Page

3.9 Horizontal farfield results 2mm away from crack tip for test 1 showing stress wave transitions by vertical line 29
3.10 Horizontal nearfield results 2mm away from crack tip for test 1 showing stress wave transitions by vertical line 30
3.11 Vertical farfield results 2mm away from crack tip for test 1 showing stress wave transitions by vertical line 30
3.12 Vertical nearfield results 2mm away from crack tip for test 1 showing stress wave transitions by vertical line 31
3.13 Split Hopkinson pressure bar raw values of test 2 with vertical lines indicating transfer of stress waves 31
3.14 Horizontal farfield results 2mm away from crack tip for test 2 showing stress wave transitions by vertical line 32
3.15 Horizontal nearfield results 2mm away from crack tip for test 2 showing stress wave transitions by vertical line 32
3.16 Horizontal nearfield results 2mm away from crack tip for test 2 showing stress wave transitions by vertical line 33
3.17 Vertical farfield results 2mm away from crack tip for test 2 showing stress wave transitions by vertical line 33
3.18 Vertical nearfield results 2mm away from crack tip for test 2 showing stress wave transitions by vertical line 34
3.19 Split Hopkinson pressure bar raw values of test 3 with vertical lines indicating transfer of stress waves 34
3.20 Horizontal farfield results 2mm away from crack tip for test 3 showing stress wave transitions by vertical line 35
3.21 Horizontal nearfield results 2mm away from crack tip for test 3 showing stress wave transitions by vertical line 35

Figure Page

3.22 Vertical farfield results 2mm away from crack tip for test 3 showing stress wave transitions by vertical line 36
3.23 Vertical nearfield results 2mm away from crack tip for test 3 showing stress wave transitions by vertical line 36
3.24 Split Hopkinson pressure bar raw values of test 4 with vertical lines indicating transfer of stress waves 38
3.25 Horizontal farfield results 2mm away from crack tip for test 4 . . 38
3.26 Horizontal nearfield results 2mm away from crack tip for test 4 showing stress wave transitions by vertical line 39
3.27 Vertical farfield results 2mm away from crack tip for test 4 showing stress wave transitions by vertical line 39
3.28 Vertical nearfield results 2mm away from crack tip for test 4 showing stress wave transitions by vertical line 40
3.29 Split Hopkinson pressure bar raw values of test 5 with vertical lines indicating transfer of stress waves 40
3.30 Horizontal farfield results 2mm away from crack tip for test 5 showing stress wave transitions by vertical line 41
3.31 Horizontal nearfield results 2mm away from crack tip for test 5 showing stress wave transitions by vertical line 41
3.32 Vertical farfield results 2mm away from crack tip for test 5 showing stress wave transitions by vertical line 42
3.33 Vertical nearfield results 2mm away from crack tip for test 5 showing stress wave transitions by vertical line 42
3.34 Split Hopkinson pressure bar raw values of test 6 with vertical lines indicating transfer of stress waves 43

Figure Page

3.35 Horizontal farfield results 2mm away from crack tip for test 6 showing stress wave transitions by vertical line 43
3.36 Horizontal nearfield results 2mm away from crack tip for test 6 showing stress wave transitions by vertical line 44
3.37 Vertical farfield results 2mm away from crack tip for test 6 showing stress wave transitions by vertical line 44
3.38 Vertical nearfield results 2mm away from crack tip for test 6 showing stress wave transitions by vertical line 45
3.39 Split Hopkinson pressure bar raw values of test 7 with vertical lines indicating transfer of stress waves 47
3.40 Horizontal farfield results 2mm away from crack tip for test 7 showing stress wave transitions by vertical line 47
3.41 Horizontal nearfield results 2mm away from crack tip for test 7 showing stress wave transitions by vertical line 48
3.42 Vertical farfield results 2mm away from crack tip for test 7 showing stress wave transitions by vertical line 48
3.43 Vertical nearfield results 2mm away from crack tip for test 7 showing stress wave transitions by vertical line 49
3.44 Split Hopkinson pressure bar raw values of test 8 with vertical lines indicating transfer of stress waves 50
3.45 Horizontal farfield results 2mm away from crack tip for test 8 showing stress wave transitions by vertical line 50
3.46 Horizontal nearfield results 2mm away from crack tip for test 8 showing stress wave transitions by vertical line 51
3.47 Vertical farfield results 2mm away from crack tip for test 8 showing stress wave transitions by vertical line 51

Figure Page

3.48 Vertical nearfield results 2mm away from crack tip for test 8 showing stress wave transitions by vertical line 52
3.49 Split Hopkinson pressure bar raw values of test 9 with vertical lines indicating transfer of stress waves 52
3.50 Horizontal farfield results 2mm away from crack tip for test 9 showing stress wave transitions by vertical line 53
3.51 Horizontal nearfield results 2mm away from crack tip for test 9 showing stress wave transitions by vertical line 53
3.52 Vertical farfield results 2mm away from crack tip for test 9 showing stress wave transitions by vertical line 54
3.53 Vertical nearfield results 2mm away from crack tip for test 9 showing stress wave transitions by vertical line 54
3.54 Split Hopkinson pressure bar raw values of test 10 with vertical lines indicating transfer of stress waves 56
3.55 Horizontal farfield results 2mm away from crack tip for test 10 showing stress wave transitions by vertical line 56
3.56 Horizontal nearfield results 2mm away from crack tip for test 10 showing stress wave transitions by vertical line 57
3.57 Vertical farfield results 2mm away from crack tip for test 10 showing stress wave transitions by vertical line 57
3.58 Vertical nearfield results 2mm away from crack tip for test 10 showing stress wave transitions by vertical line 58
3.59 Split Hopkinson pressure bar raw values of test 11 with vertical lines indicating transfer of stress waves 58
3.60 Horizontal farfield results 2mm away from crack tip for test 11 showing stress wave transitions by vertical line 59

Figure Page

3.61 Horizontal nearfield results 2mm away from crack tip for test 11 showing stress wave transitions by vertical line 59

3.62 Vertical farfield results 2mm away from crack tip for test 11 showing stress wave transitions by vertical line 60

3.63 Vertical nearfield results 2mm away from crack tip for test 11 showing stress wave transitions by vertical line 60

3.64 Split Hopkinson pressure bar raw values of test 12 with vertical lines indicating transfer of stress waves 61

3.65 Horizontal farfield results 2mm away from crack tip for test 12 . 61

3.66 Horizontal nearfield results 2mm away from crack tip for test 12 showing stress wave transitions by vertical line 62

3.67 Vertical farfield results 2mm away from crack tip for test 12 showing stress wave transitions by vertical line 62

3.68 Vertical nearfield results 2mm away from crack tip for test 12 showing stress wave transitions by vertical line 63

3.69 Fracture envelope showing angles of 15° 30°, 45° and 60° measured from the horizontal direction 66

A.1 Free body diagram on a triangular surface at an angle 77

Acronyms

CTOD crack tip opening displacement. v, xv, 11, 12, 26

DIC Digital Image Correlation. v, 13, 18, 24–28, 67

LEFM Linear Elastic Fracture Mechanics. 10, 11, 67, 69

SHPB split-Hopkinson pressure bar. v, 6, 9, 13, 15–17, 20, 26–28, 67, 77, 78

NOMENCLATURE

VARIABLES	UNITS	DESCRIPTION
U	mm	Horizontal CTOD
V	mm	Vertical CTOD
σ	N/m^2	Stress
Y	Unitless	Geometry factor
a	mm	Starter crack length
K	$MPa\sqrt{m}$	Stress intensity factor
K_I	$MPa\sqrt{m}$	Mode I fracture toughness
K_{II}	$MPa\sqrt{m}$	Mode II fracture toughness
k_{stress}	Unitless	Plane stress conditions
β	radians	Angle of weakened plane from the horizontal
x_c	mm	Distance from crack tip

GREEK SYMBOLS	UNITS	DESCRIPTION
E	N/m^2	Elastic modulus
μ	N/m^2	Shear modulus
ν	mm	Poisson's ratio

CHAPTER I

Introduction

1.1 The dynamic behavior of materials

Since the dawn of human existence, the dynamic behavior of materials has played an important role in every aspect of life and development. During the Prehistoric Period, humans utilized dynamic fracturing of rock by the means of flint knapping to make spears and knives to hunt and develop. In 1453, Mehmed II victory over the byzantine empire was largely achieved by the dynamic power of cannons to impact and cause damage to Constantinople's defensive walls. During the great and second world wars, the use of dynamic fracture was greatly studied to make developments to military weapons and transport vessels to take impacts from artery from hostile forces. Dynamic behavior of materials even plays a role in automotive safety and space shuttle designs to prevent catastrophic failure from collisions. The dynamic behavior of materials is critical to the understanding of earthquakes and the minimization of damage caused by earthquakes, and even has applications in the extraction of oil and natural gas. For example, shale, which makes up 70% of the earth's crust, is highly susceptible to dynamic impacts since the materials contain weakened planes in the form of repetitive layering of grains in metamorphic rocks. This splitting is known as foliation and is very useful for the petroleum industry due to the ability to allow oil to transfer through the grains when fractured during unconventional extraction. The ability to fracture rock to extract petroleum has become so achievable in shale regions that an abundant amount of land is available for the continuation of unconventional petroleum

extraction, U.S. Energy Information Administration (2022); Mohr and Evans (2011) and accounts for 70% of the world's total petroleum reserve, He et al. (2015). This makes shale the second-largest mean source of oil and gas Fahem and Singh (2021). However, the extraction of shale petroleum can fall by 60%-90% in the first year of production, Jia et al. (2016). This decline is due in part to shale oil extraction having an average of only 3-7% recovery due to the viscosity and capillary forces preventing flow through rock fractures, U.S. Energy Information Administration, U.S. Department of Energy (2015).

This decline in production is in part caused by the lack of understanding of shale fracture in regards to its complexity as a layered material. This misunderstanding is primarily due to the stress wave interactions along weakened planes in shale regions and the angle at which these stress waves interact with the layers' weakened plane. Several Studies have been conducted on weakened planes in regards to shale characterization. Luo et al. (2018) determined the shale characteristics using a three-point bend test inside a scanning electron microscope to determine the stress intensity factor of four different bedding inclination angles for Longmaxi shale and compared the result to similar literature. Tan et al. (2018) utilized numerical simulations to determine the strain energy release rate on coal specimens and that the degradation of the mechanical properties and their weakened effect significantly depends on the bedding angle between the bedding planes and load direction. This research goal was to understand the dynamic-static loading in terms of the strain energy release rate and did not mention the mixed mode interactions of the stress waves or the stress intensity factor. Meier et al. (2015) used shale specimens to determine the formation of borehole breakouts shale by using emission sensors and strain gauges of shale at various bedding angles. However, this was done on a quasi-static experimental apparatus and stress wave interactions were not discussed. The studies neglected mode II failure because the numerical re-

sults determined that the stress concentration factor for the shear component was less than 5% for each bedding inclination angle. However, the mode II component for dynamic interactions contributes substantially to the failure mechanics of brittle materials. This research neglected the mode II failure characteristics, in the quasi-static case. However, when looking at dynamic fracture, it is expected that Mode two fracture will play an important role in the failure characteristics in shale. Thus, the dynamic interaction is still not understood.

Dynamic behavior of materials play a major role in 3D printing due to the interaction of subsequent layers of filaments when printing. There has been a push to develop 3D printers in construction to build houses with concrete as the filament. The 3D printing of concrete allows for easier and cheaper laying and design of houses and walls. As of now, construction-related spending is 10 trillion globally, making it one of the largest sectors in the world economy, Sanjayan and Nematollahi (2019). However, the need for more advanced construction is required for modern development and rising house costs. In Oklahoma, a house valued at $200,000 has increased to 134.0%- 144% depending on the fiscal quarter from 1991 to 2019, United States Department of Labor (2019b). This mixed with wages in Oklahoma's minimum wage has only increased 62% from 1991 to 2019, United States Department of Labor (2019a), making it increasingly difficult for the young population to buy homes. 3D printing houses can lower costs of housing, reduce construction waste, increased safety for construction operations, reduced labor cost, and reduced construction error, making construction more sustainable than traditional construction operations, Afolabi et al. (2019). However, 3D printing has many flaws that need to be studied before large-scale operations can take place. One primary reason for this is due to subsequent layering boundaries of concrete causes weakened planes to develop. There have been multiple studies that attempt to

characterize this process. For example, Li et al. (2020) discussed fracture along weakened planes of 3D printed concrete with micro-cable reinforcing methods. It was shown that weak interfaces created by the printing path affect the shear strength considerably due it the initiation of an accumulation of cracks at the interface of the concrete specimen. It was found that printing configuration will create the weakest resistance to fracture when the planes are parallel shearing planes and the strongest resistance to fracture when the weak planes are perpendicular to the shear stresses. The geopolymer weak planes' directions between the two filaments is the largest characteristic that determines the shear strength, Li et al. (2020). In a different research, with the same goal of creating a usable 3D printed concrete, Sanjayan et al. (2018) looked weak inter-layer strength between 3D printed layers vs. cast and mold. The weak inter-layer strength of printed concrete is a limiting issue for the construction industry due to the adhesive bonding of extruded layers which is dependent on delay time, Sanjayan et al. (2018). Le et al. (2012b) discussed the effects of anisotropic voids in layered structures in regards to filaments to weaken the structural capability interfaces. The components of concrete are dependent on the bond filament and between layers, Le et al. (2012a). Emmanuel Keita Keita et al. (2019) discusses origins of weakened planes in 3D printed concrete and found that the result of low porosity of fresh concrete between laying new layers is the result of the weakened plane. The liquid is not able to wet the concrete in a constant manner leaving dry regions that act as weakened planes on the material. The research for 3D printing has an interest in weakened planes in the form of anisentropic voids creating acting as stress concentration factors and the layering causing a weakened plane. However, the leap into the stress wave interactions of these voids within the weakened planes has not been discussed.

One of the last mentioned applications in weakened plane fracture is seen in

composite materials. Composite materials have one of the widest applications in any industry. They are used in aeronautics, automotive, and sports equipment due to light-weight and high-strength applications. Composites have an interest with layered structures because of the inherent properties between the matrix and fibers. The study of stress wave propagation in composites began in the 70s and continued for five decades. Some of the early work for stress wave propagation in composites was done by Barker (1971) when he developed a theoretical model to describe stress wave propagation through a composite material using a viscous model with success. Another early research was done by Lundergan and Drumheller (1971), the researchers also looked at laminated plate composites through a dual experimental and analytical study. The experimental consisted of the use of a compressed flat gun to accelerate a flat plate to induce a planar impact. The analytical portion consisted of two computer programs to analyze the wave propagation through the composite. The first consisted of TIC which uses a simple-centered, finite differenced form of a linear equation. The second program was WONDY III. This general Lagrangian wave-propagation program generates solutions one dimensional, finite difference equations of motion, mass, and energy of continuum mechanics. The results showed that the peak amplitude of the stress wave decreased directly with the width of the input stress pulse. However, a majority of the stress reduction was based on reflections of the stress wave at the left and right sides of the composite boundaries. Some of the more recent research was completed by Barouni and Rekatsinas (2021). This research studied the stress wave propagation in flax fiber-reinforced composite strips using two different techniques. The first utilizes a layer-wise theory for the through-the-thickness displacement field an analytical expression of the displacement along the length of the strips. These are then compared to a time domain spectral finite element method. The goal of the research was to detect any changes in the waves as it

propagates along layered complex structures and was found to give an accurate description of the stress wave. Tasdemirci et al. (2004) looked at two and three layered glass/epoxy composites and its effects on stress wave propagation. A SHPB was used to test two and three layered materials with the goal to explain dynamic deformations of multilayered composites and the conform modeling results. In addition, strain gauges were utilized to validate the model. The numerical simulation, LS-DYNA, was shown to have successful results for modeling SHPB tests on multilayer composite materials. It was found that wave propagation characteristics was not noticeably effected by the placement of impedance layers. However, when rubber was placed in the middle of the two major structural layers, it was shown that there is a reduction in the maximum stress in every layer. Also, there was an inhomogeneous and changing stress distribution within the layers. Within composite research, there have been studies for stress wave interactions across interfaces that act as weakened planes. The effects of angles of weakened planes are not discussed.

Whether it be through brittle shale fracture, 3D printing, or composite materials, all applications have a need for the understanding of stress wave interactions along weakened planes. Despite of the wide applications of stress wave interactions, the study of stress wave response to weakened planes at angles has not been studied in great detail. This research will describe the effects of stress waves interactions on angled weakened planes in the presence of central cracks on polycarbonate specimens with cyanoacrylate at the weakened plane. A weakened plane in this study is used as a broad term that includes any direct and clear change in material characteristics caused by a physical or chemical change that runs through a plane in a material. For composite materials, the weakened plane can be the interface between the matrix and fiber, for 3D printed materials the weakened plane is the layers that form between passes during manufacturing, and for shale the weakened plane is

caused by material changes between layers. Regardless of the origin of the weakened plane, the fracture characteristics are controlled by numerous factors such as cracks in the material, the mode of fracture, the amount of elastic and plastic deformation the material can withstand, and the strain rates applied to the material.

1.2 Stress wave interactions and strain rates

Stress wave interactions in materials have a substantial impact on the material response. This is especially true when cracked, weakened planes, are present. Stress waves are defined as a mechanical wave that causes disequilibrium in a solid resulting in the solids particles adjusting to accommodate the stress and achieving equilibrium. When a material is disturbed, whether it be by a person skipping a stone across a lake, a spring compressing, or a musician strumming a string on a ukulele, mechanical energy is transferred. This energy will propagate from the initial disturbance and propagate into the material. This propagation will disturb equilibrium conditions on the material until all the energy has been dissipated into the material. This dissipation can only exist when elasticity and inertia effects are taken into consideration. If elasticity and inertia effects are neglected, the result in the material is never able to accept mechanical energy and transfer this energy past the surface. Assuming the former is the case, this energy will transfer as a wave through the material and if high enough will cause fracture of the material.

The study of waves propagation through a material has been studied for thousands of years with the earliest recorded back to about 500 BC when when the Greek brotherhood of Pythagoras experimented with the goal of obtaining the musical pitch of a vibrating string and in regards to its length. Since then, due to the versatility of stress waves and its applications to so many fields of science, mathematics and engineering. Some of the most notable studies on

stress waves have been done by Daniel Bernoulli (1700-1784), Joseph Lagrange (1736-1813), Lord Rayleigh (1842-1919), E.F.F. Chladni (1756-1829), Sophie Germain (1776-1831), C.L.M.H. Navier (1785-1836), Augustin Cauchy (1789-1857), Simeon Denis Poisson (1781-1840), Heinrich Hertz (1857-1894), and Sir Horace Lamb (1849-1934) studied a collection of issues in relation to stress waves. This varied from vibrations in plates, beams, vibrations of strings, wave propagation in the earth and the periodic movement of the cosmos Selvadurai (2013); Lamb (1917); Hertz (1882); J J O'Connor and E F Robertson (2002).

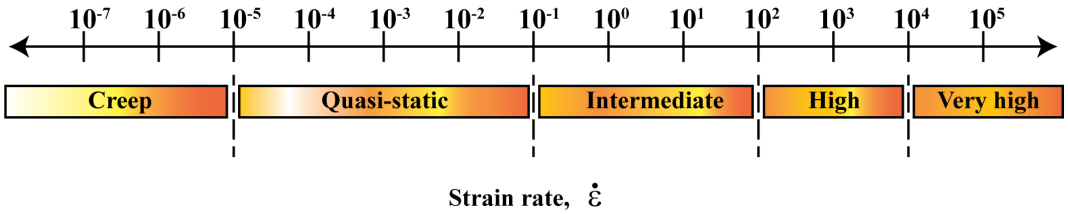

Figure 1.1: Number bar showing the effects strain rates for different loading conditions

The mechanical stress wave response is limited to strain. Since hooks law describes stress and strain being proportional to one another by the elastic modulus, it is challenging to measure the stress wave response without the material undergoing a mechanical deformation. Strain is more commonly looked at in the form of strain rates, that is, the time at which strain occurs. Strain rate dictates materials response to stress and is broken into five categories: Creep, Quasi static, Intermediate, High, and Very High. These strain rates are shown linearly in figure 1.1. First, creep strain is small strain rates in the range of $\leq 10^{-5}$. This is commonly seen in wood when a constant weight is applied. Over time, the weight of the object will begin to bend the wood. This type of strain conditions is only possible if the object is placed on the wood for long periods of time which will result in long term deformations. The second is most common is seen in tensile testing, this is done for tests ranging in the proximity of $10^{-5} \leq 10^{-1}$. The third is intermediate strain rates, this is seen as the beginning region into dynamic strain rates of $10^{-1} \leq 10^{2}$. An

example of this would be john Hopkinson's drop weight experiments Hopkinson and Hopkinson (1901) as described in section 2.2. The fourth section is in the range of $10^2 \leq 10^4$ and covers elastic and plastic stress wave response in materials. This strain rate is seen on the SHPB and is the chosen method for this research. The SHPB and its uses are discussed in depth in sections 2.1 and 2.2. The fifth is very high strain rates and is seen as everything equal to and above 10^5. This blast impact and is commonly utilized in shock wave propagation or explosions.

1.3 Mixed mode fracture interactions

When strains are applied to a material, energy is being stored regardless of the strain rates. A material has a maximum energy that can be withheld and after the maximum amount of energy is exceeded, the material will fracture. There are three categories of fracture that determines the fracture path behavior of a material and is based on the orientation of the crack tip. The first known as mode I fracture and is when the principal load is applied normal to the crack plane as shown in Figure 1.3 (a) The second is mode II fracture and is the in plane shear loading is the sliding of one side of the crack face with respect to the other as shown in Figure 1.3 (b). The third and final mode of fracture is mode III, as shown in Figure 1.3 (c). This corresponds to out of plane shear loading and is not discussed in detail in this paper due to the nature of the experimental apparatus requiring that the out of plane forces be negligible.

It is common in engineering practices that modes of fracture be mixed together in combinations. For example, in the auto industry, hot mix asphalt will experience all three modes of failure simultaneously from vehicles passing over the asphalt Ameri et al. (2011). Another example is soda lime glass which accounts for 90% of all manufactured glass Robertson (2005). This

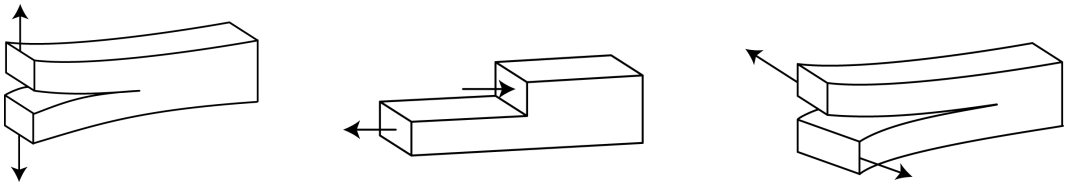

(a) Mode I: opening fracture showing the direction of loading

(b) Mode II: shearing fracture showing the direction of loading

(c) Mode III: tearing fracture showing the direction of loading

Figure 1.2: The three modes of fracture with directional loading

glass commonly exposed to a mix of mode I and Mode II fracture. Ayatollahi and Aliha (2009). These fracture types are known as mixed mode fracture and falls under the superposition principle that allows for mode I and mode II to be algebraically quantified together. This quantity is the total amount of needed energy absorption to fracture a specimen under mixed loading conditions. The major similarity between the soda lime glass, hot mix asphalt is that these materials fall under Linear Elastic Fracture Mechanics (LEFM). The benefit of LEFM is that it describes the fracture characteristics of brittle materials or materials that have very low plastic deformation and can employ linear elastic relations between stress and strain. In other words, Hooks Law is valid.

1.4 Stress wave response in the presence of cracked bodies

Stress wave interactions will change based on the materials characteristics that allow for stress transfer through a material. For example, 1.3a, shows a block passing a force through a material with no defects, the force lines will pass through the material with no interruptions if ignoring boundary conditions. Similarly, if there is a weakened plane in the block, 1.3b, there would be the same interactions as the block shown in 1.3c even though a weakened plane is present. The force lines are able to travel through the median that is the weakened plane. However, if a crack is added to this weakened plane, the force lines no longer have a median to pass through and will travel though the

block to the nearest point of contact, in this case the crack tip, and will build creating a stress concentration.

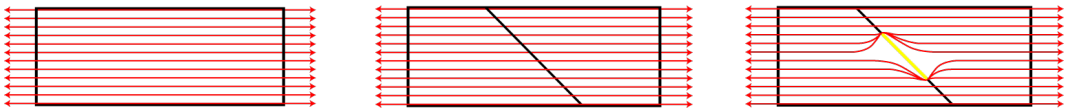

(a) Plane Bock with no weakened plane or crack showing force lines

(b) Block with angled weakened plane showing force lines

(c) Block with angled weakened plane and crack showing force lines

Figure 1.3: Force lines though a block

However, the stress concentration factor is a geometric parameter and not able to provide material based answers. This means whether the material is steel, wood, plastic or rock, the stress concentration would be the same as long as the geometry constraints are the same. For this reason, the fracture toughness is used in this study, since it provides both material characteristics and failure properties.

1.5 Crack tip opening displacement and plastic zone

When a material contains a crack, as shown in 1.3c, the crack tip experiences stress singularities that would require the crack to propagate spontaneously as soon as a crack develops by definition of LEFM. However, much of the time, this is not the case. Stress singularities at the crack tip exist, and the application of LEFM collapses leaving a small region that prevents spontaneous crack propagation. This region is shown in 1.4 as the dashed red circle and is responsible for keeping the material together when a crack develops. This region does not follow the LEFM model and attempting to analyze with this model will end in inconsequential results.

In response to this phenomenon, it is important to analyze near the crack tip but so not so close that the point is in the plastic region of the crack tip. To account for the plastic zone, a parameter known as the crack tip opening displacement (CTOD), and is a crucial component to understand crack tip

parameters. The CTOD is defined as two 45° degree lines from opposite sides of the crack tip as shown in 1.4 and when the 45° lines intercept with crack tip boundaries are the crack tip opening points. The distance of the crack tip opening can be used to characterize loading conditions near the crack tip and be related back to the stress intensity factor.

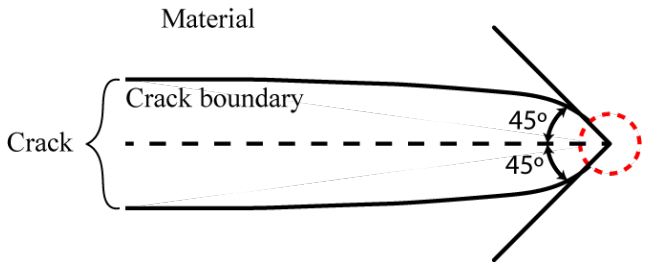

Figure 1.4: Crack tip and path showing 45° lines with plastic zone

CHAPTER II

Experimental Setup

2.1 Components of the experimental apparatus

There are two independent experimental techniques used in this study. The first is a SHPB and the second is high speed camera method using DIC. The setup for this experiment is shown in Figure 2.1 for the SHPB and the DIC is shown in Figure 2.2. The setup and the components for both apparatuses are bulleted below:

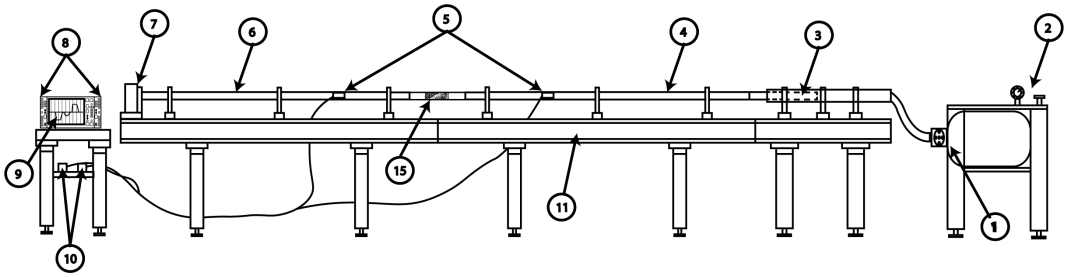

Figure 2.1: Not to scale split Hopkinson pressure bar testing schematic

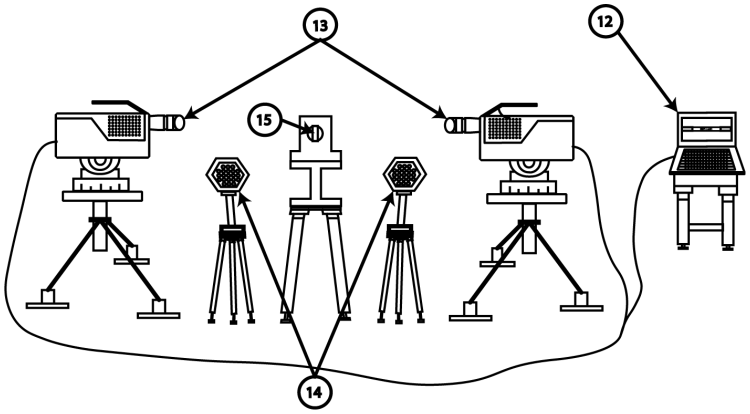

Figure 2.2: Not to scale digital image correlation and camera testing schematic

1. Air tank
2. Release valve
3. Striker bar
4. Incident bar
5. Strain gauges
6. Transmitted bar
7. Stop block
8. Amplifiers
9. Oscilloscope
10. Wheatstone bridge
11. I-beam
12. Computer
13. High speed cameras
14. Lights
15. Specimen

This experimental procedure uses a loaded pressure vessel released into the gas gun which will launch the striker bar into the end of a incident bar to generate an elastic wave, known as the elastic wave. The incident wave will travel through the incident bar to the specimen. The discrepancy of the mechanical impedance from the incident bar and the specimen will cause a portion of the incident wave to be reflected back into the incident bar as a reflected wave and the remainder of the incident wave broadcasts through the specimen, which compresses the specimen at high rates in the order of 10^2 to 10^4, into the transmitted bar and is known as the transmitted wave. Both the transmitted, incident, and reflected waves are sensed by two quarter Wheatstone bridge strain gauges attached to the incident and transmitted bars and documented on an oscilloscope and amplifiers. The aluminum bars are used to allow appropriate amplification of the pressure waves and allow for appropriate, non-dispersive, one dimensional, and elastic wave propagation into the specimen.

During the elastic wave propagation between the incident bar, specimen, and transmitted bar, a high speed camera is taking photos of the speckled

specimen to input into digital image correlation, as shown in Figure 2.3 for farfield and Figure 2.4 for nearfield. The face of the specimen is speckled to allow the camera to record the displacement of the individual speckles on the face of the specimen, shown in Figure 2.5. The cameras were placed on opposite sides of the specimen to capture farfield and nearfield displacements. The farfield encompasses the field of view to capture the whole specimen resulting in a variable length and the nearfield with a approximate 20mm localized field of view of the crack and crack tip. The cameras and oscilloscope was set to record every microsecond.

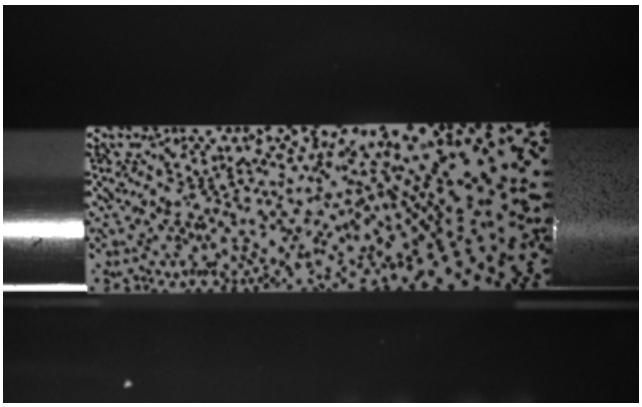

Figure 2.3: Farfield image of a 60 degree test

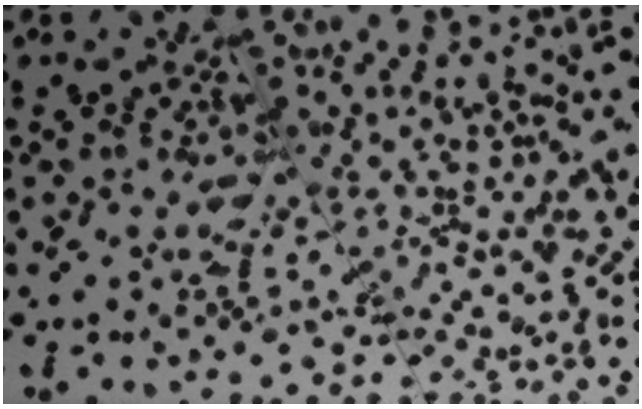

Figure 2.4: Nearfield image of a 60 degree test

The SHPB has a 2133.6mm (7 ft) incident and transmitted bar both at one inch diameter. The striker bar is one foot with the same 25.4mm (1 in) diameter and all bars are made from T7075 aluminum. A MDO32 3 series

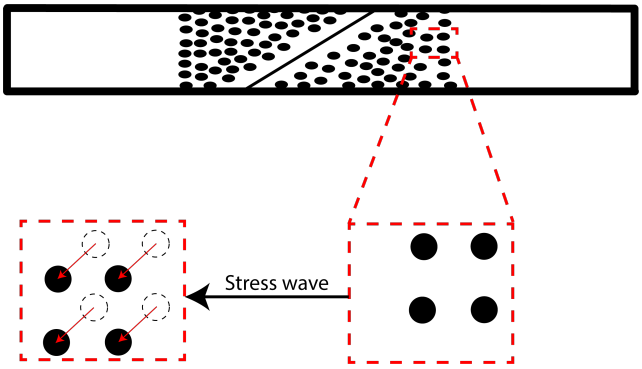

Figure 2.5: Movement of nearfield speckle on specimen captured by DIC

mixed domain oscilloscope and two Vishay 2310B signal conditioning amplifiers are used to capture the elastic waves. The recording method used are two HPV-2X Shimadzu high speed cameras and the lighting system consists two Rez Hex-700W systems. The specimen details are explained in depth in 3.1

2.2 Brief history of the split-Hopkinson pressure bar

The SHPB has a lengthy development that has many variations due to its versatility as a testing apparatus. The SHPB saw major development during the years of the first and second world war due to its applications in dynamic propagation and its uses dynamic material response. Below a summary of the history of the SHPB and a timeline bar chart is shown in Figure 2.6.

In 1872, John Hopkinson conducted drop weight experiments on an iron wire. This research revealed that regardless weight of the dropper, the speed is what dictated whether the fracture of the wire would initiate at the impact end or the the fixed end; Hopkinson and Hopkinson (1901). John Hopkinson's research was one of the first to characterize a material's response based on speed of an impact. Later, John Hopkinson's son, Bertram Hopkinson, developed a pressure bar to measure the pressure produced by high speed bullets. This apparatus allowed Bertram Hopkinson to create a pressure-time curve created from the impact; Hopkinson (1914). In 1847, R. M. Davies preformed a validation on the Hopkinson bar using parallel plates and cylindrical con-

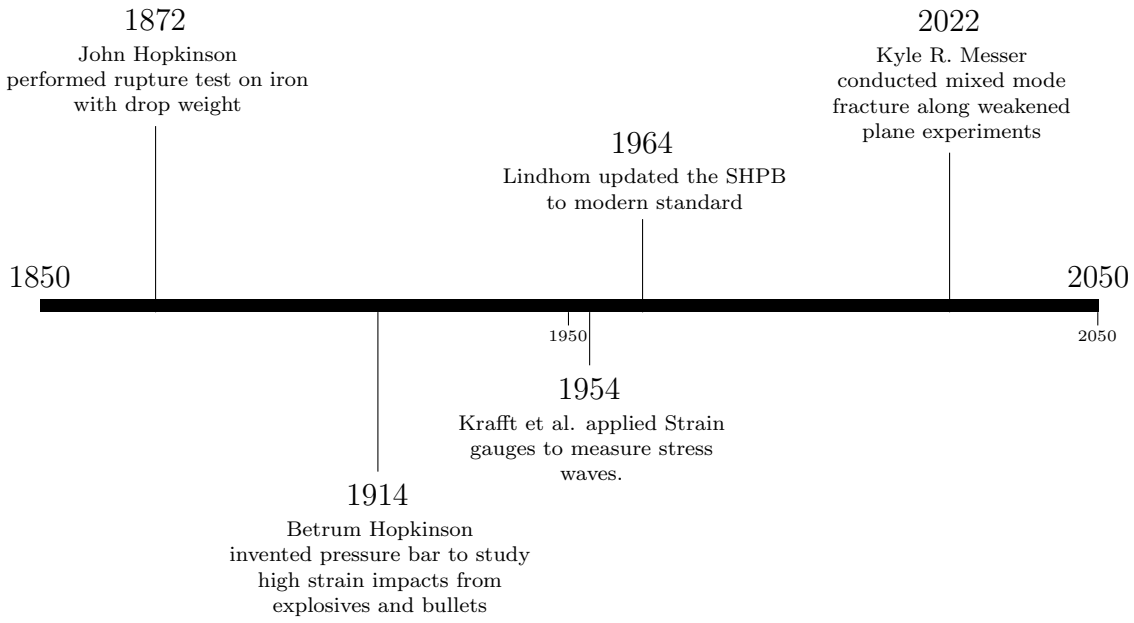

Figure 2.6: Timeline of the development of split Hopkinson pressure bar

densers microphones to measure the pressure as a function of time from bullet impact; Davies and Taylor (1948). Davies work is some of the earliest work to use electronics as a measurements tool on the Hopkinson bar and showed that electronics are more accurate than the method Bertram Hopkinson developed. This lead to Kolsky to develop the the two bar apparatus along with the parallel plates and cylindrical condensers microphones developed by Davies to measure stress-strain materials response at the high strain rates for a variety of materials such as cooper, rubber, polythene, and lead; Kolsky (1949). In 1954, Krafft utilized strain gauges in place of parallel plates and cylindrical condensers microphones to measure strain waves. Also, in place of an explosive detonator Krafft used a gas gun to launch a projectile or more commonly known as the striker bar; Krafft et al. (1954). Lindholm summarized and updated this work to what is now the modern times SHPB for dynamic

characterizing; Lindholm (1964).

2.3 Brief history of digital image correlation

DIC falls into the category of science known as photogrammetry. Photogrammetry is derived from three Greek words: phos, gramma, and metrein. phos is the word for light, gramma is the word for a letter or something being drawn, and metrein means to measure. The definition of photogrammetry is the use of photography in surveying and mapping to measure distances between objects.

The origins of photogrammetry begins with the consideration of using perspective and imagery and can be found as early 1480 by Leonardo da Vinci and his studies in 1492; Gruner (1977); Doyle (1964) with some debate that the idea dates even farther back as the Greeks; Center for Photogrammetric Training (2020). In 1525, Albrecht Duerer, successfully build an device that could create a true perspective drawing; Bigun (2006). In the 1600's Christian Huygens created the magic lantern, one of the earliest forms of slide projectors, by use of candles and glass to create moving images; Magic Lantern Society (2020). These developments gave way to Heinrich Lambert to make mathematical developments for perspective and imaging by use of space resection to locate a point in space from an image in his treatise "Perspectiva Liber" (The Free Perspective, 1759); Center for Photogrammetric Training (2020); Sutton et al. (2009). Daguerre in 1837 with material from Niepce created the first practical photographic images from Iodine, silver plates and silver covered copper plates. The latent image was then treated after exposure effectively bring out the photo; Marien (2006).

This lead into the improvement of phase of imaging. This period was broken into four sections; Sutton et al. (2009); Konecny (1985). These sections, as mentioned by Sutton in; Sutton et al. (2009) are plane photogrammetry which includes 1850 through 1900, analog photogrammetry which includes

1900 though 1950, analytical photogrammetry that includes 1950 through 1985) and digital photogrammetry which dates from 1985 and is still currently in use. The method of gaining material deformation measurements acquired from computer-based image acquisition was first developed by Peters and Ranson in 1982; Peters and Ranson (1982); Sutton et al. (2009). Several other developments and refinements were made to image based material deformation measurements whcih are referenced here; Sutton et al. (1983); Peters et al. (1983); Chu et al. (1985); Tian and Huhns (1986).

CHAPTER III

Methods

3.1 Specimen preparation

The specimen was designed to ensure a fully developed stress wave by the time the wave reaches the centrally cracked weakened plane and prevents undesired amplification from material and geometry mismatch. Polycarbonate was chosen for its high impact resistance to ensure the weakest point of the specimen is the cyanoacrylate weakened plane. The specimen was chosen to have a height of 25.4 mm. This is the same as the diameter as the SHPB. The specimen and bar diameter will prevent any change in the wave geometry, amplification, and stress concentration effects. The specimens length was chosen to have a length of at least 25.4 mm from the start of the weakened plane. The minimal length allows adequate distance for the wave to become fully developed by time the wave reaches the weakened plane. The specimen geometry was chosen to be rectangular which allows uniform loading to occurs and provides that the wave characteristics to remain uninterrupted when the wave travels through the incident bar onto the specimen. A starting crack length of 6.35mm was selected to provide adequate weakened plane distance for the 25.4 mm height of the specimen and to guarantee crack propagation of the weakened plane.

The preparation of the specimen began with a sliding compound miter saw (Ryobi® TSS103) to rough cut large sheets of Tuffak® polycarbonate (McMaster-Carr®). The specimen was then precision cut with a milling machine (Accupath AC-3KV) and a three-flute mill bit (Speed Tiger® Iaue 1/2" 3) with a water-cooling spray system (OriGlam 130103020Q) as the coolant

Table 3.1: Material properties of cyanoacrylate

Property	Value	Units
Elastic Modulus	1.33	GPa
Shear Modulus	0.48	GPa
Poisson's Ratio	0.40	Unitless

for the machining process. A three-way precision angle vise was used to cut the specimen at the desired 15, 30, 45, and 60, 75 angles. The creation of the specimen is shown in Figure 3.1-3.6. The specimen after after machining is shown in Figure 3.1 and Figure 3.2. The specimen was then glued together using a Loctite glue (Loctite® Super Glue Liquid Brush 5 gr 852882 en-US) that creates the weakened plane seen in Figure 3.3. The general properties of cyanoacrylate are shown in table 3.1 based on data taken from Komurlu et al. (2016). The brush on superglue allows for a uniform coating to be spread across the weakened planes while preventing unwanted spreading of glue to the crack. TaegaSeal PTFE tape was used to create a starter crack that spanned equally across both sides of the specimen. The specimen was spray-painted using (Rust-Oleum® Painter's Touch® 2X Ultra Cover336098 Flat White) and allowed to dry completely, shown in Figure 3.4. A fine tip sharpie (Sharpie® 37101PP) was used to hand speckle the specimen the back side of the specimen and the farfield side was speckled using a bold sharpie (Sharpie® 30051) and the results are showing in Figures 3.5 and 3.6 respectably. The difference sizes of the speckle from the farfield and nearfield side of the specimen is to gain more precise results based the field of view of the cameras. The farfield data will require larger speckle patterns while the nearfield will require smaller speckles based on the resolution and clarity of the images.

Figure 3.1: Cut specimen

Figure 3.2: Corner view of taped specimen

Figure 3.3: Specimen glued with starter crack

Figure 3.4: White base on specimen

Figure 3.5: Farfield specimen

Figure 3.6: Nearfield specimen

3.2 Assumptions and sources of error

The viability of these experiments relies on several assumptions as bulleted below with a brief explanation of the importance of these assumptions.

1. Uniform bonding in specimens.

   Uniform bonding in specimens is required due to ensure steady state transfer of stress waves across the weakened planes.

2. Equal bonding distance.

   Equal bonding distance is required two keep uniformity in specimen preparation and stopping any eccentric effects in the loading conditions

3. Bonding is sufficient to uniformly transfer stress waves.

   The bonding of the two sides needs to uniformity transfer stress waves and no localized point loading conditions are created by the passing of stress waves.

4. Rigid body inertial effects are negligible.

   As the angle of the weakened plane becomes less, the specimen will become longer to keep the one inch distance between bar and weakened plane. This will result in inertial effects on the longer specimens and, in turn, a mismatch in accuracy in each angle of weakened planes.

5. The 25.4mm distance between weakened plane and bar are sufficient to allow a steady and fully developed stress.

   A uniform and steady state stress wave is required to gain true stress wave interactions across the specimen. If this is not the case, then the wave has transient conditions and the values are not valid.

6. Two points are within tolerable measures to give accurate stress wave interactions at the crack tip.

These experiments are based on two points alone from the DIC. The general consensus is that a full field tests set from the DIC will give best results.

7. No compressive forces were generated from the bonding in the glue. Another issue that needs to be considered is the force required to bond the specimens together without causing, When glueing the specimen together, it is required to press the left and right side of the weakened planes together. The goal was to push them together enough to ensure uniform bonding but allow the weakened planes to bond under a compressive force.

3.3 Theory of equations for the split Hopkinson pressure bar

The equations for the dynamic stress intensity factor, $K_{I,II}(t)$ follow the general central crack problem shown in equation 3.1. A geometry factor, Y, is needed to account that the crack is in the inclined weakened plane. The inclined crack will create a mixed mode problem between the opening mode I and the shearing Mode II.

$$K_{d,I,II}(t) = \sigma(t) * Y * \sqrt{\pi * a} \tag{3.1}$$

The first parameter needed is to relate the general central crack to the inclined plane. This is achieved through a geometry factor. To determine the geometry factor, a force balance at a point is employed on the specimen can be utilized. A free body diagram is shown in figure A.1 with the balance point chosen to be at the middle of the inclined plane as depicted in yellow. A deviation is shown in APPENDIX A of the geometry factor and the final results with with the stress intensity factor for $K_I(t)$ and $K_{II}(t)$ being represented with equations 3.2 and 3.3 respectably. These standard equations are shown and

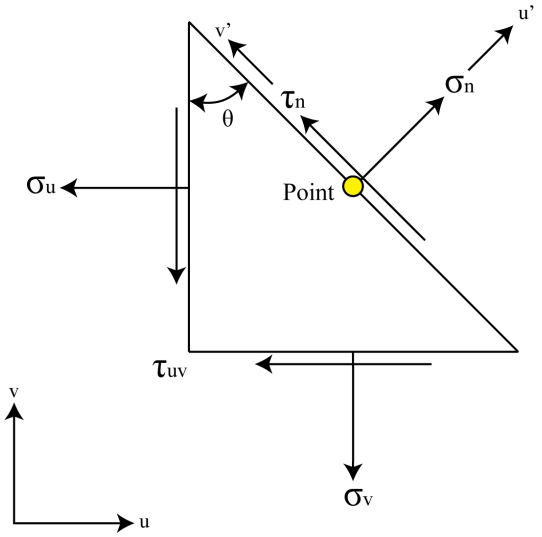

Figure 3.7: Free body diagram on a triangular surface at an angle

deviated in equations 2.43a and 2.43b from Anderson and Anderson (2005).

$$K_I(t) = \sigma(t) * sin(\beta) * sin(\beta) * \sqrt{\pi * a} \tag{3.2}$$

$$K_{II}(t) = \sigma(t) * cos(\beta) * sin(\beta) * \sqrt{\pi * a} \tag{3.3}$$

Mixed mode fracture equation follows the law of vector addition or Pythagorean's theorem as discussed in section 1.3.

$$K_{mixed}(t) = \sqrt{K_I(t)^2 + K_{II}(t)^2} \tag{3.4}$$

3.4 Theory of equations for digital image correlation

The stress intensity factors are calculated from the DIC displacements using modified equations from 4a and 4b presented in "A CTOD-based mixed-mode fracture criterion" by Ma et al. (1999), and are deviated using general equations of crack surface displacement methods as shown by Sun and Jin (2011) in the book Fracture Mechanics. The equations 4a and 4b are shown again and are rearranged for the stress intensity factor in equations 3.5 and 3.6 and account

for a main crack coordinate system.

$$K_I(t) = \frac{(U_1 - U_0)}{\frac{k_{Stress}+1}{\mu} * \sqrt{\frac{x_c}{2*\pi}}} \tag{3.5}$$

$$K_{II}(t) = \frac{(V_1 - V_0)}{\frac{k_{Stress}+1}{\mu} * \sqrt{\frac{x_c}{2*\pi}}} \tag{3.6}$$

However, the equations 3.5 and 3.6 need to be slightly modified to account for the equations being developed along the main crack instead of globally across the specimen. The equations used to calculate the stress wave interactions at the crack tip across weakened planes are shown in equations 3.7 and 3.8. Where the sine and cosine are a function of weakened plane angle and allow for the equations to be used globally across a weakened plane specimen.

$$K_I(t) = \frac{(U_1 - U_0) * cos(\beta)}{\frac{k_{Stress}+1}{\mu} * \sqrt{\frac{x_c}{2*\pi}}} \tag{3.7}$$

$$K_{II}(t) = \frac{(V_1 - V_0) * sin(\beta)}{\frac{k_{Stress}+1}{\mu} * \sqrt{\frac{x_c}{2*\pi}}} \tag{3.8}$$

The goal of the DIC is two fold, to gain CTOD measurements to attain stress wave interaction properties and determine fracture toughness values. This is achieved by placing two high speed cameras on opposite sides of the weakened planes. The first camera is placed to have a field of view of the whole specimen and the second camera is placed to have a field of view of 20mm to give localized information. These two methods are compared with each other and with transmitted bar values from the SHPB that gives global fracture toughness values.

3.5 Results

The method of experimentation has three forms of results, farfield, nearfield, and SHPB. Each angle will have a farfield, nearfield, and SHPB graphs that show the history of the stress wave interactions along the specimen.

The SHPB, raw values generated from the transmitted bar on the SHPB are plotted as shown in figures 3.8- 3.64 as the beginning of each individual test set. There are three lines of stress wave history. The first line is start of elastic compression, the second is the end of elastic compression and transitions to shear forces on the specimen, the third and final line is the fracture point and is the fracture toughness value. Every point beyond fracture point, is based on how the material is able to transfer the stress wave after fracture. For example, if the specimen wedges, it will still be able to transfer the stress wave even though it has fractured.

In terms of the farfield and nearfield data, the first vertical line shows the initial interaction from the bar to the specimen. The wave has passed through the specimen but has not interacted with the weakened plane. The second line is the start of elastic compression. This is when the stress wave interacts with the weakened plane causing the right and left side of the specimen to compress together making the weakened planes compress. The third line is the end of elastic compression and start of shear forces on the specimen. When the specimen can no longer compress from the weakened planes, the weakened plane will begin to slide along the weakened interface causing shear fracture. The fourth and final line is the fracture point and is the fracture toughness value. Every point beyond the fracture point is post fracture and will change based on whether the two fracture sides wedge together, slide, or attach to each other. The farfield and nearfield have two sets of results, horizontal and vertical, from the DIC. The horizontal data is shown in figures 3.10-3.66 and 3.9-3.65 as the second and third of each individual test set respectively. The

farfield and nearfield vertical graphs are shown in figures 3.12-3.68 and 3.11-3.67 as the fourth and fifth of each individual test set respectively.

The DIC nearfield and farfield sees longer vertical stress wave movement compared to the horizontal stress wave movement. This is caused by the boundary conditions of the transmitted and incident bar in the horizontal direction. The vertical direction has no boundary conditions that leave the specimen to rigidly deform. The cause of the DIC nearfield and farfield data having four sets of distinguishing lines and the SHPB having three sets of distinguishing lines is a result from the nature of the experiments. The DIC is able to see deformation across the specimen before interaction across the weakened plane while the transmitted wave values from the SHPB only measures from one point which are the strain gauges. It should also be noted that the specimens will, by design, always fail by shear forces. This is due to the the bulk of the polycarbonate material having a tremendously higher ability to accept stress waves than the weakened cyanoacrylate planes and is seen in the disparity of the other angles when compared to the 75° specimens.

The raw values are shown in a tabular setting. The data is setup in three groups of two tables. The three groups are broken into angle of the weakened plane. The first table is a section of three experiments with the critical fracture toughness displayed. The second table is the average of the three tests with a standard deviation of the nearfield data.

3.6 The 15 degree results

Three specimens were tested at 15° angles were completed, the results showed that the primary mode of failure Mode I direction and minimal mode II failure.

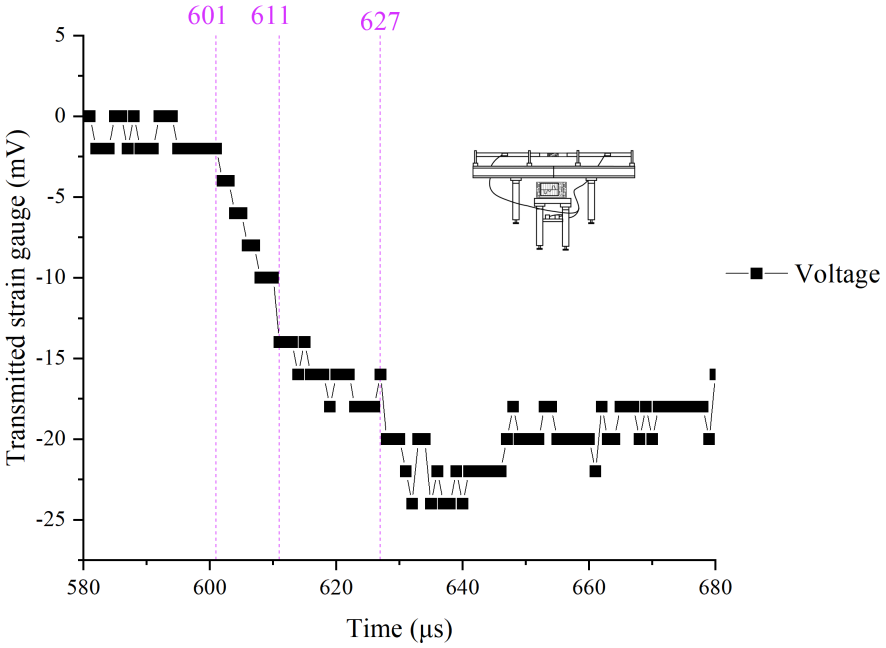

Figure 3.8: Split Hopkinson pressure bar raw values of test 1 with vertical lines indicating transfer of stress waves

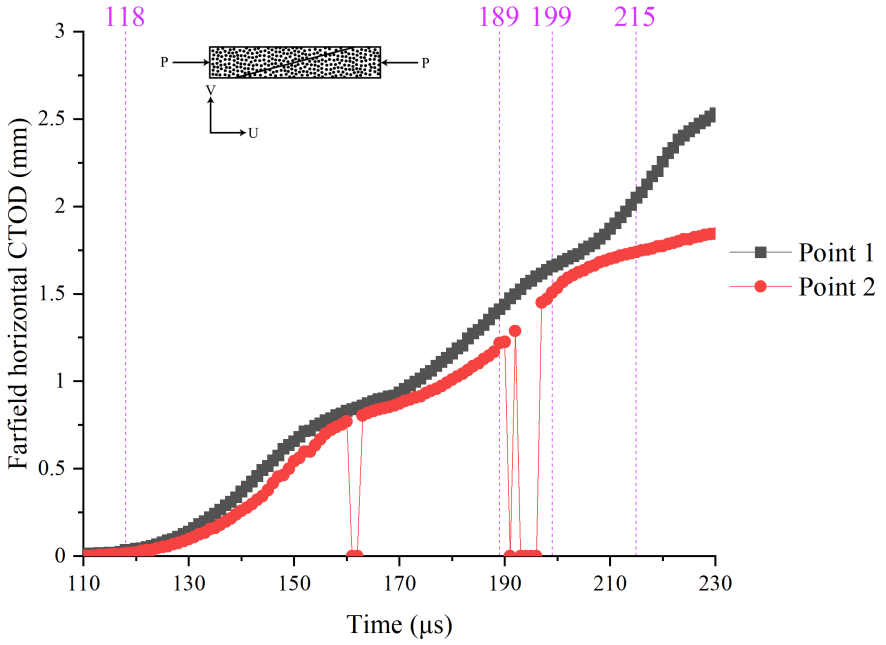

Figure 3.9: Horizontal farfield results 2mm away from crack tip for test 1 showing stress wave transitions by vertical line

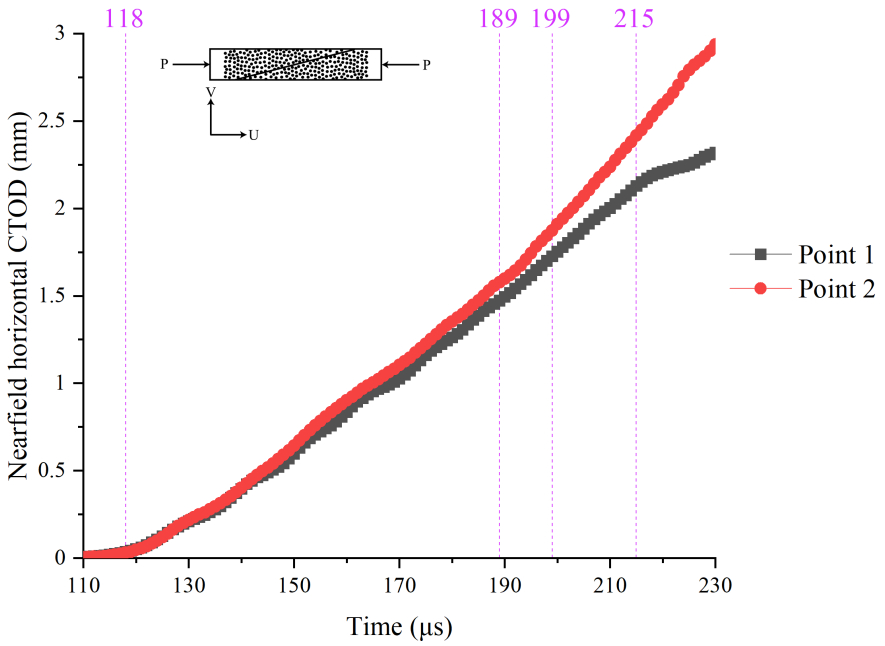

Figure 3.10: Horizontal nearfield results 2mm away from crack tip for test 1 showing stress wave transitions by vertical line

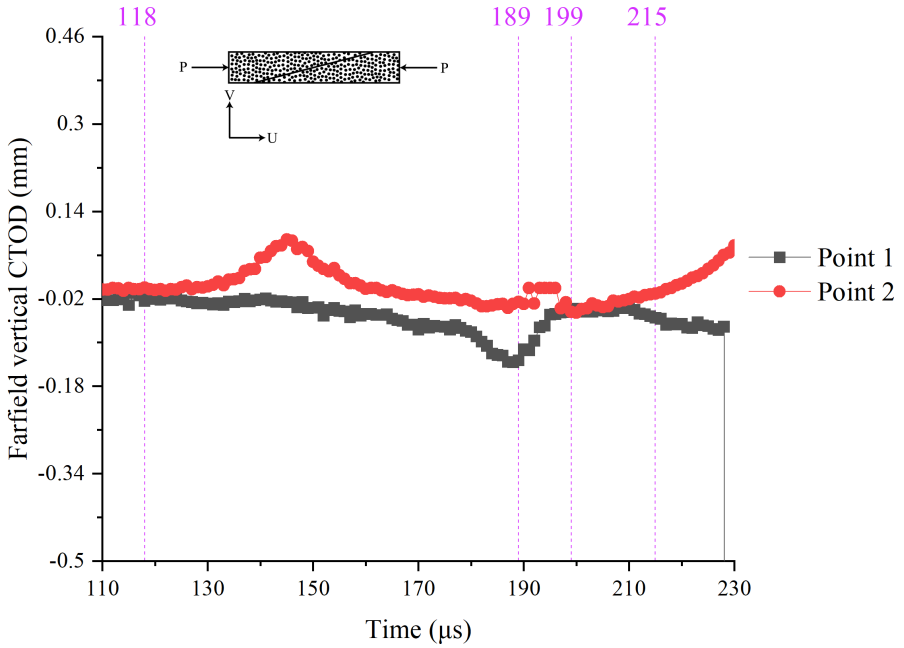

Figure 3.11: Vertical farfield results 2mm away from crack tip for test 1 showing stress wave transitions by vertical line

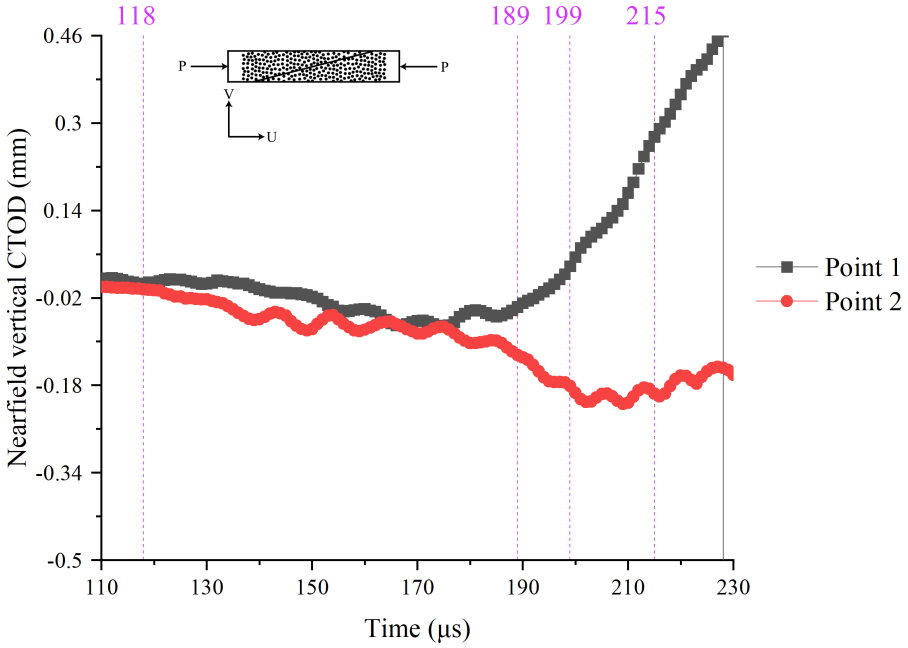

Figure 3.12: Vertical nearfield results 2mm away from crack tip for test 1 showing stress wave transitions by vertical line

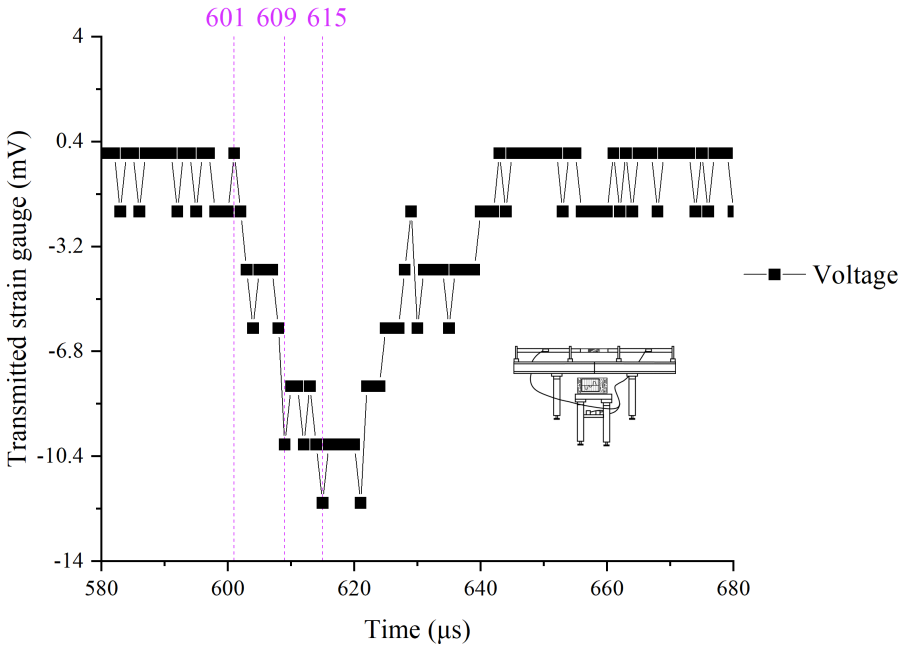

Figure 3.13: Split Hopkinson pressure bar raw values of test 2 with vertical lines indicating transfer of stress waves

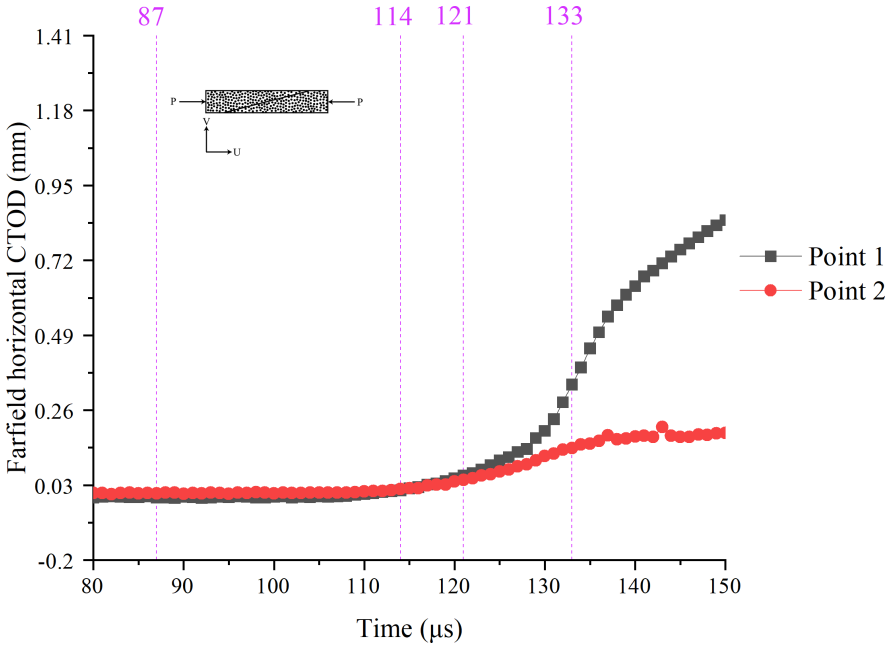

Figure 3.14: Horizontal farfield results 2mm away from crack tip for test 2 showing stress wave transitions by vertical line

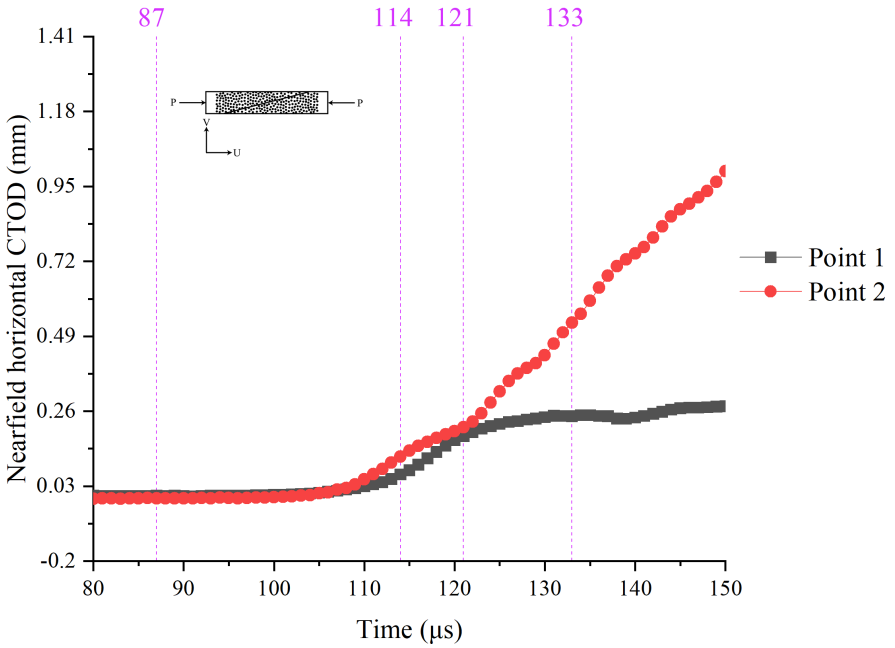

Figure 3.15: Horizontal nearfield results 2mm away from crack tip for test 2 showing stress wave transitions by vertical line

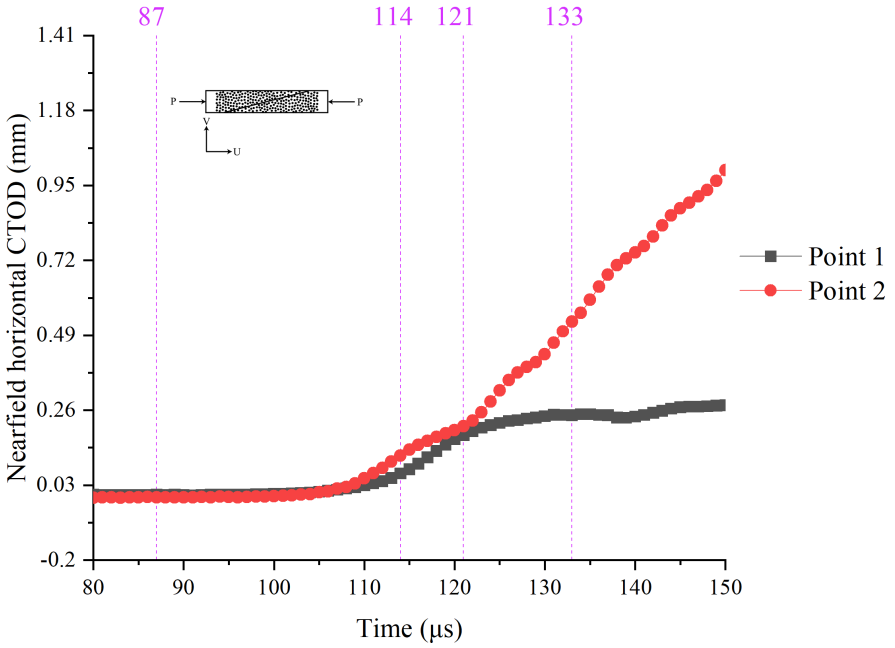

Figure 3.16: Horizontal nearfield results 2mm away from crack tip for test 2 showing stress wave transitions by vertical line

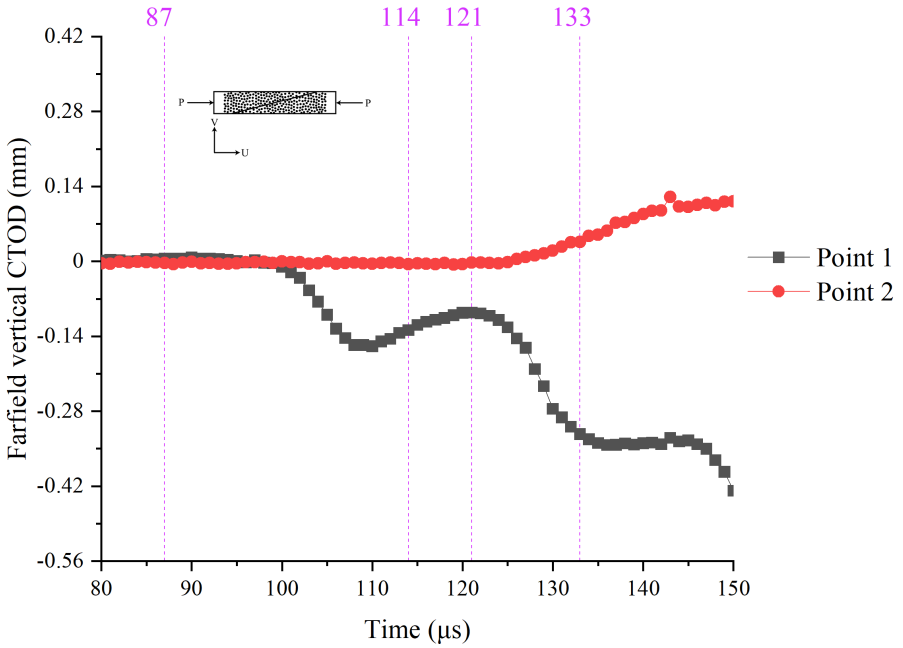

Figure 3.17: Vertical farfield results 2mm away from crack tip for test 2 showing stress wave transitions by vertical line

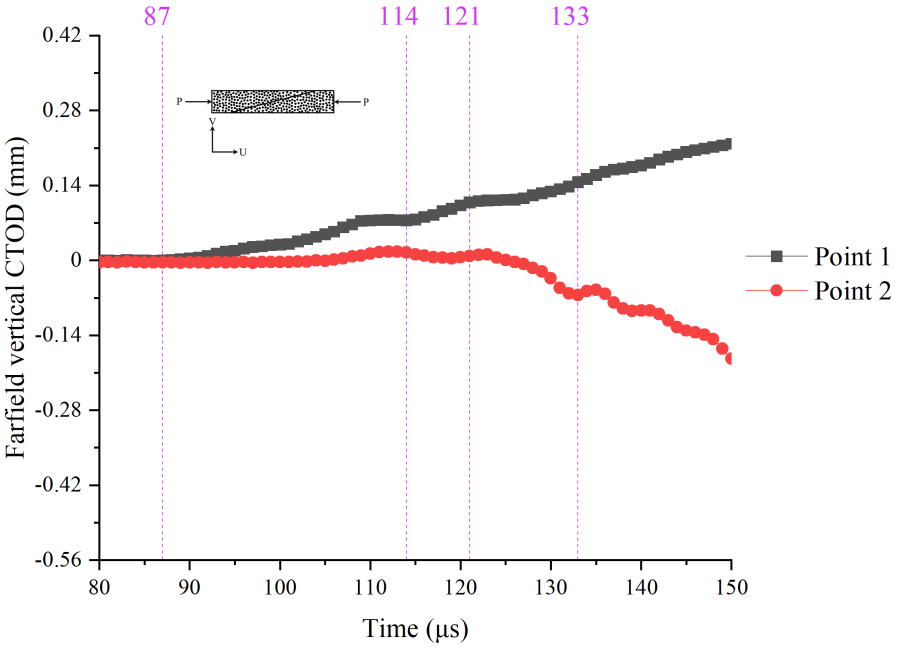

Figure 3.18: Vertical nearfield results 2mm away from crack tip for test 2 showing stress wave transitions by vertical line

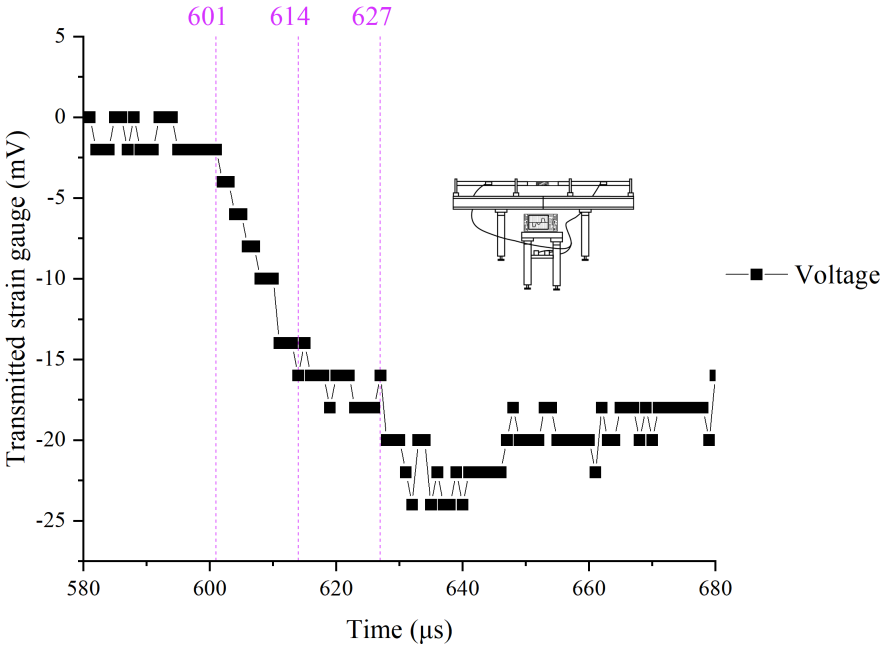

Figure 3.19: Split Hopkinson pressure bar raw values of test 3 with vertical lines indicating transfer of stress waves

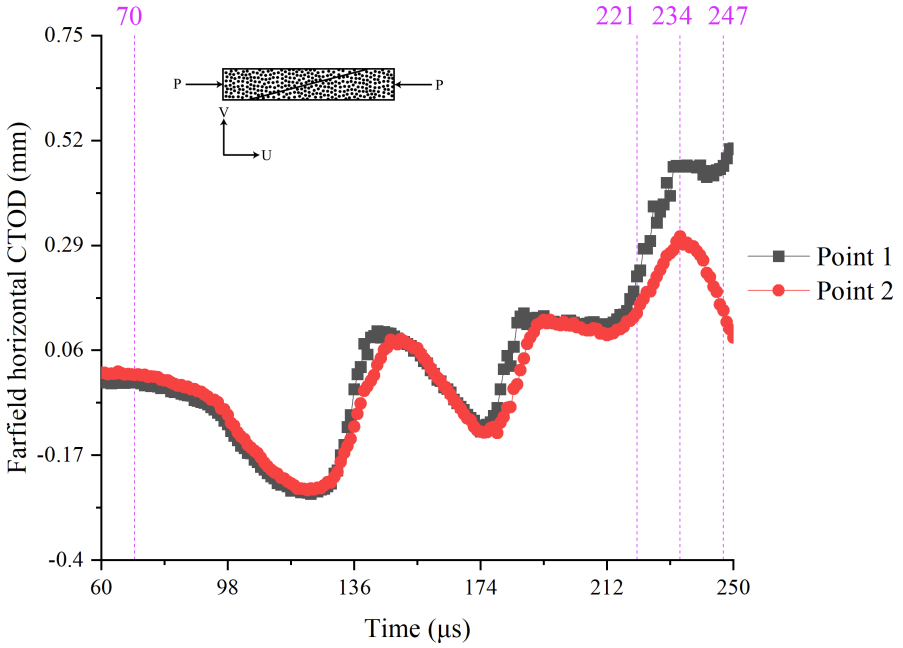

Figure 3.20: Horizontal farfield results 2mm away from crack tip for test 3 showing stress wave transitions by vertical line

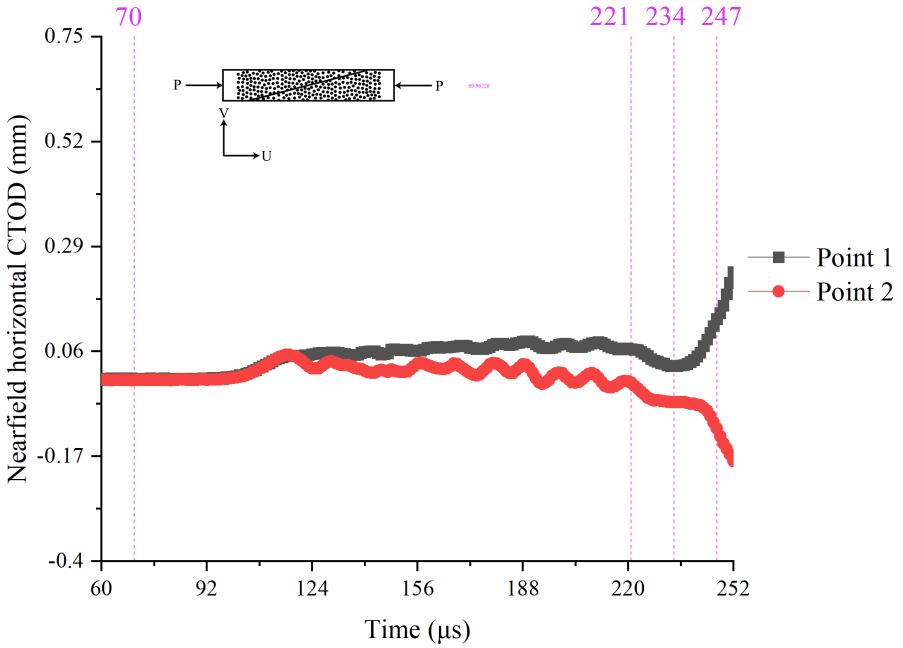

Figure 3.21: Horizontal nearfield results 2mm away from crack tip for test 3 showing stress wave transitions by vertical line

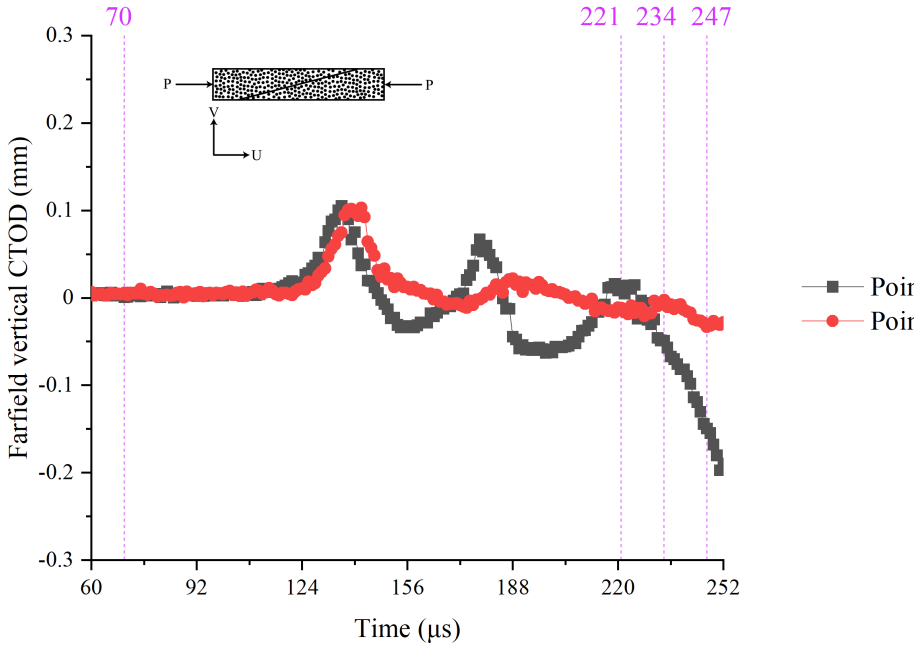

Figure 3.22: Vertical farfield results 2mm away from crack tip for test 3 showing stress wave transitions by vertical line

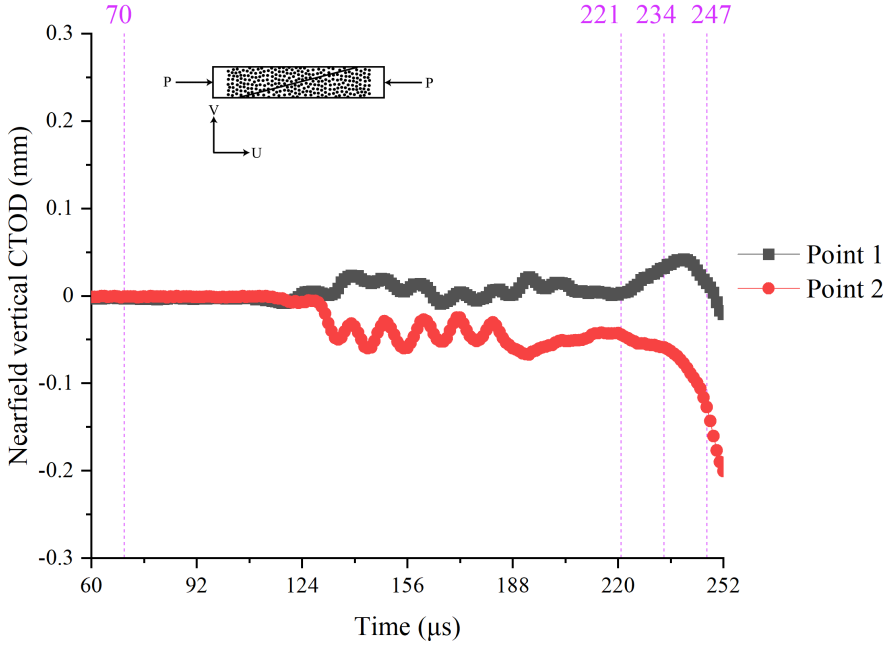

Figure 3.23: Vertical nearfield results 2mm away from crack tip for test 3 showing stress wave transitions by vertical line

Table 3.2: Polycarbonate along centrally cracked weakened planes dynamic fracture toughness for a weakened plane angle of 15°

Specimen #	**Fracture Mode**	**Farfield** $MPa\sqrt{m}$	**Nearfield** $MPa\sqrt{m}$	**SHPB** $MPa\sqrt{m}$
1	$\boldsymbol{K_{d,I}}$	1.94	1.69	1.76
	$\boldsymbol{K_{d,II}}$	0.20	0.25	0.47
	$\boldsymbol{K_{d,Mixed}}$	1.95	1.71	1.82
2	$\boldsymbol{K_{d,I}}$	1.49	1.98	1.32
	$\boldsymbol{K_{d,II}}$	0.31	0.19	0.35
	$\boldsymbol{K_{d,Mixed}}$	1.52	1.99	1.37
3	$\boldsymbol{K_{d,I}}$	2.02	1.53	1.76
	$\boldsymbol{K_{d,II}}$	0.20	0.24	0.47
	$\boldsymbol{K_{d,Mixed}}$	2.03	1.55	1.82

3.7 The 30 degree results

Three specimens were tested at 30° angles were completed, the results showed that the primary mode of failure Mode I and minor mode II failure.

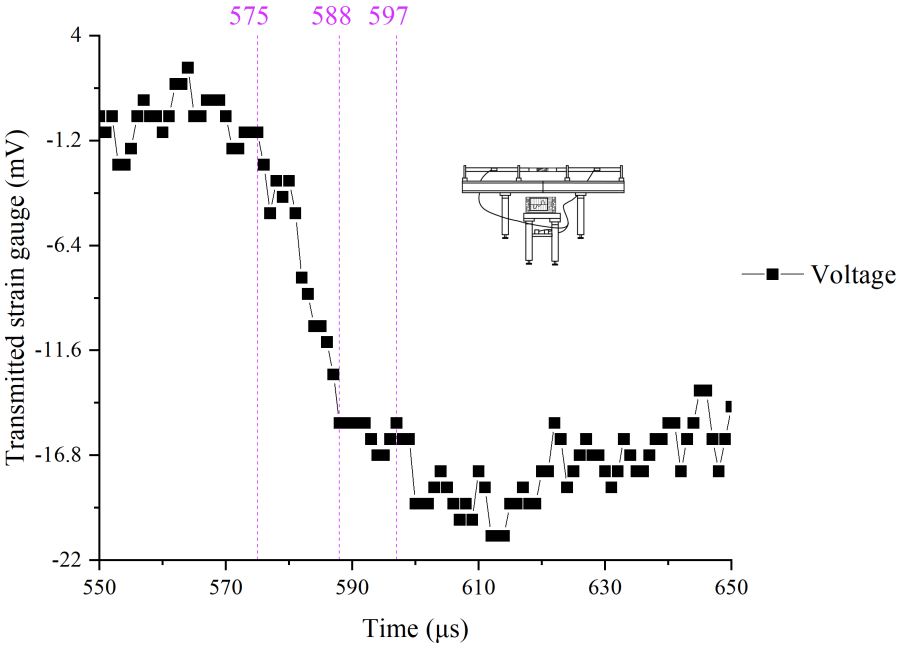

Figure 3.24: Split Hopkinson pressure bar raw values of test 4 with vertical lines indicating transfer of stress waves

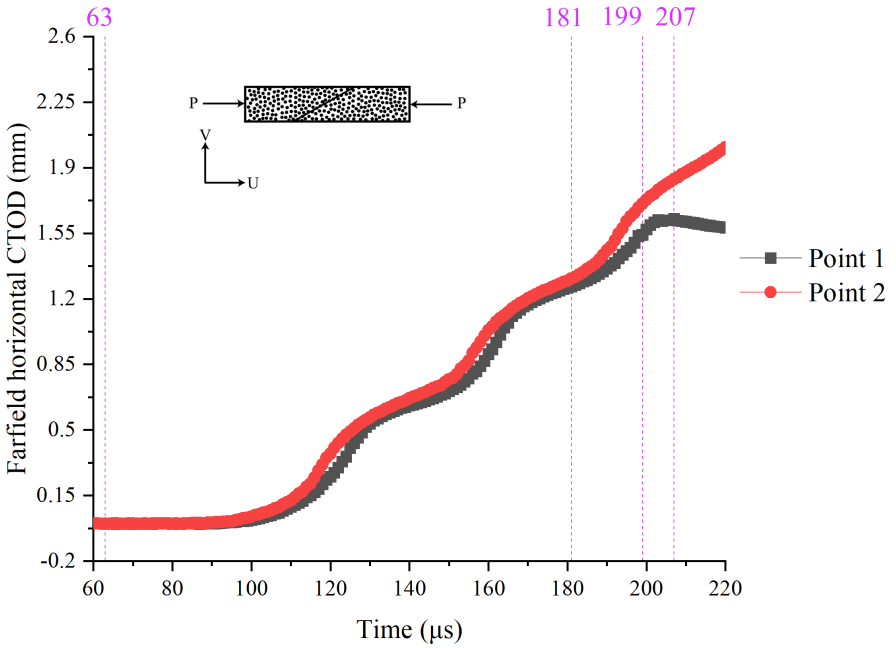

Figure 3.25: Horizontal farfield results 2mm away from crack tip for test 4

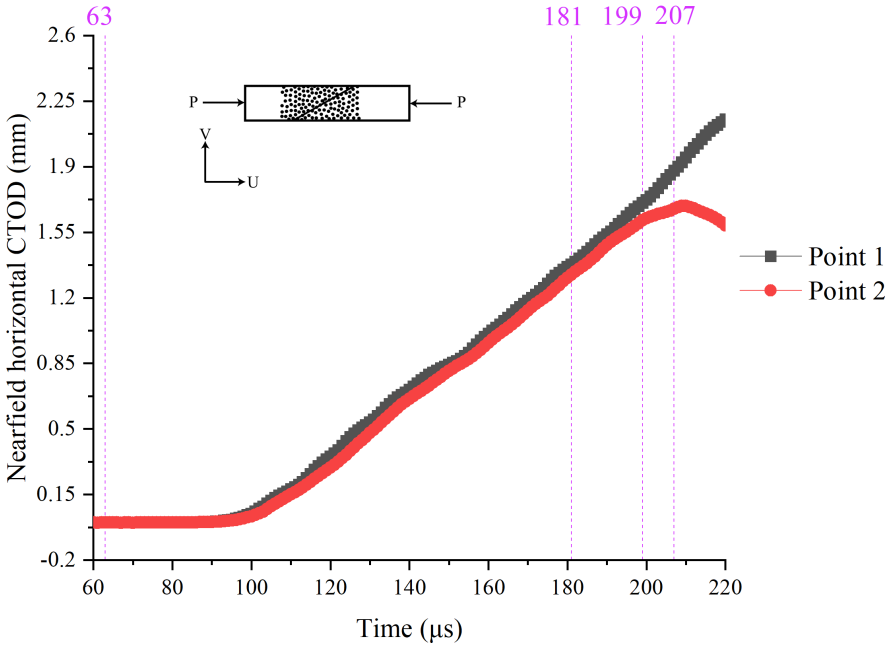

Figure 3.26: Horizontal nearfield results 2mm away from crack tip for test 4 showing stress wave transitions by vertical line

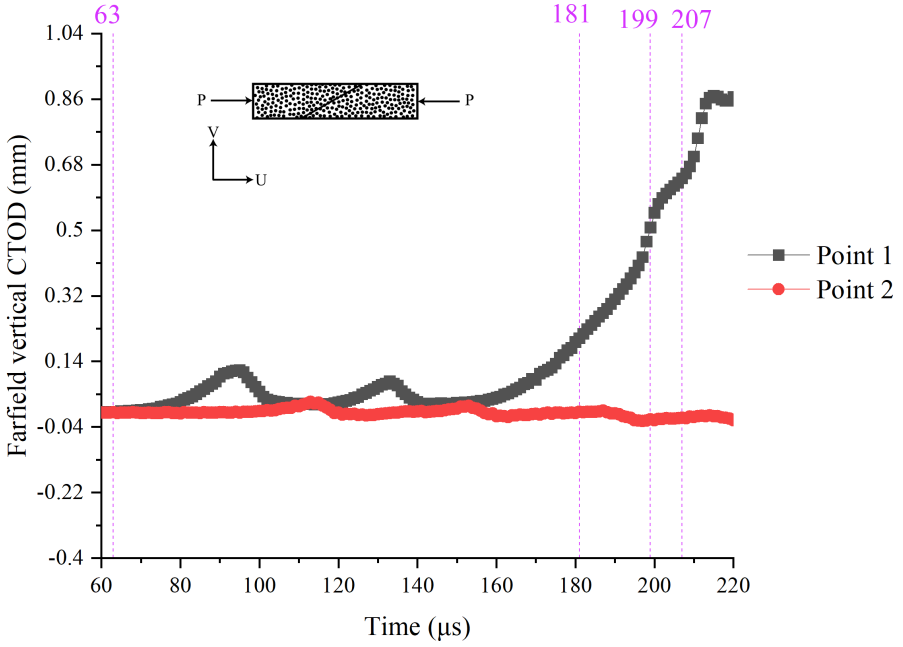

Figure 3.27: Vertical farfield results 2mm away from crack tip for test 4 showing stress wave transitions by vertical line

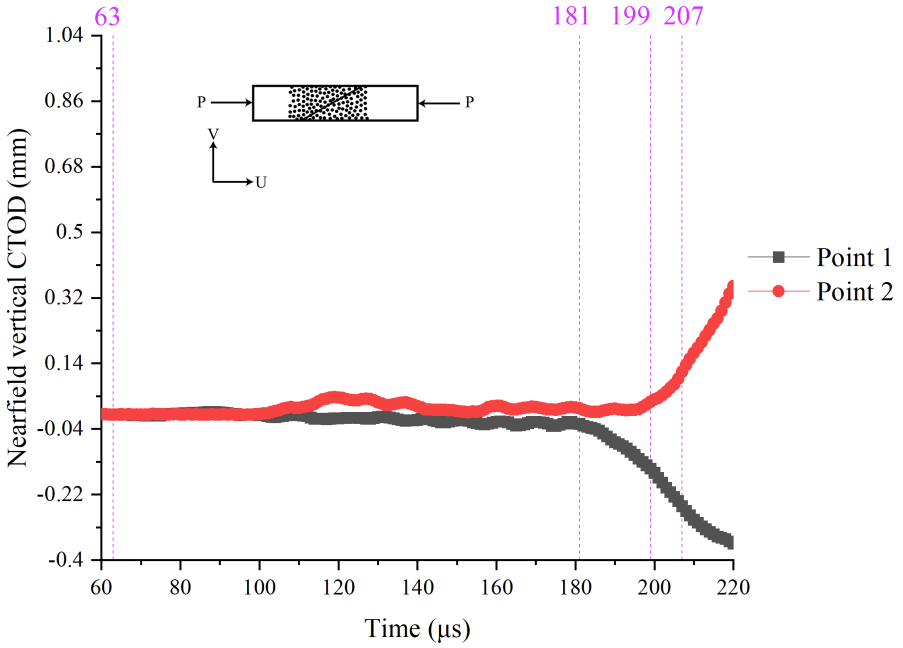

Figure 3.28: Vertical nearfield results 2mm away from crack tip for test 4 showing stress wave transitions by vertical line

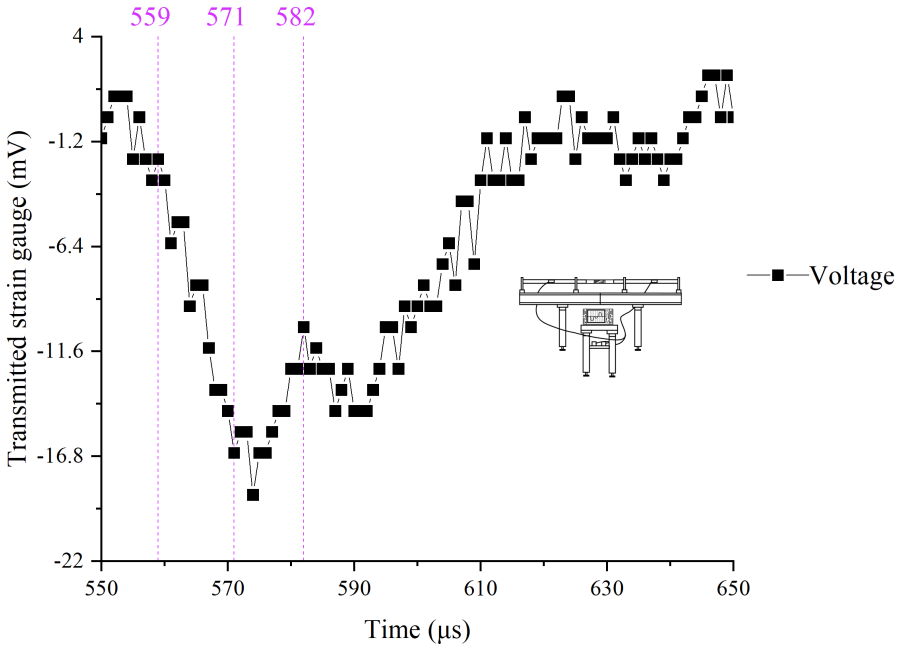

Figure 3.29: Split Hopkinson pressure bar raw values of test 5 with vertical lines indicating transfer of stress waves

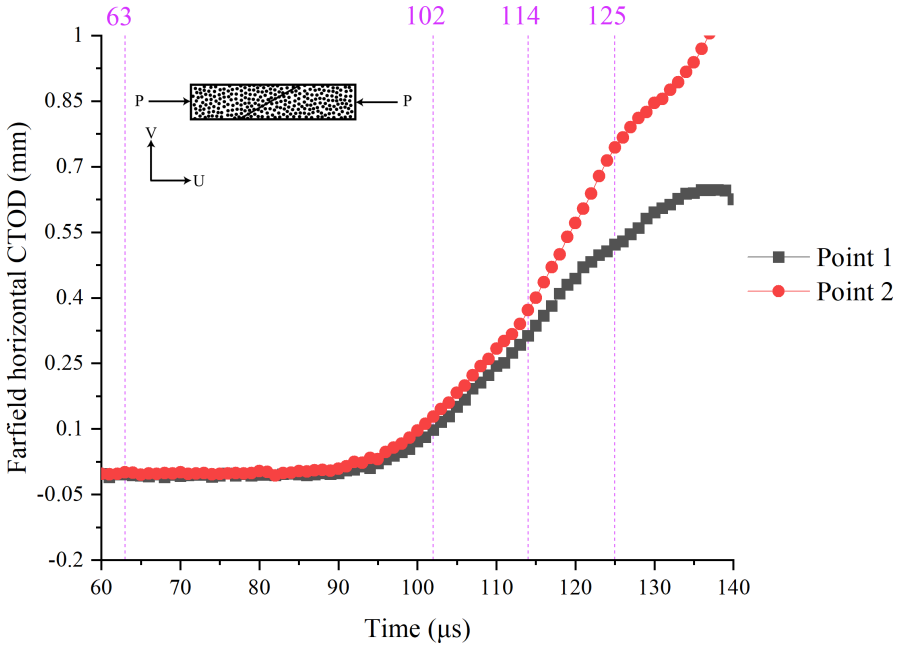

Figure 3.30: Horizontal farfield results 2mm away from crack tip for test 5 showing stress wave transitions by vertical line

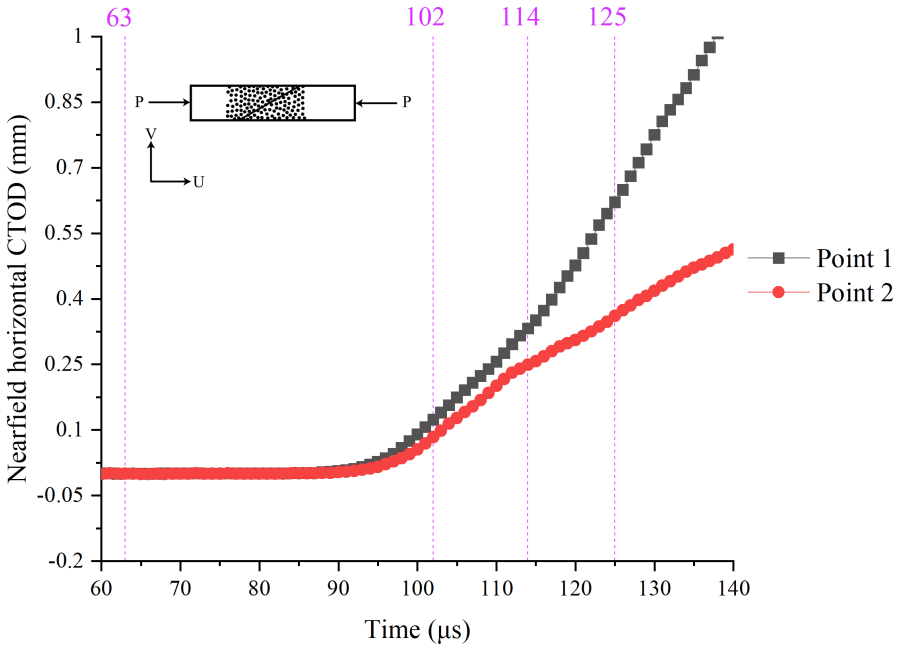

Figure 3.31: Horizontal nearfield results 2mm away from crack tip for test 5 showing stress wave transitions by vertical line

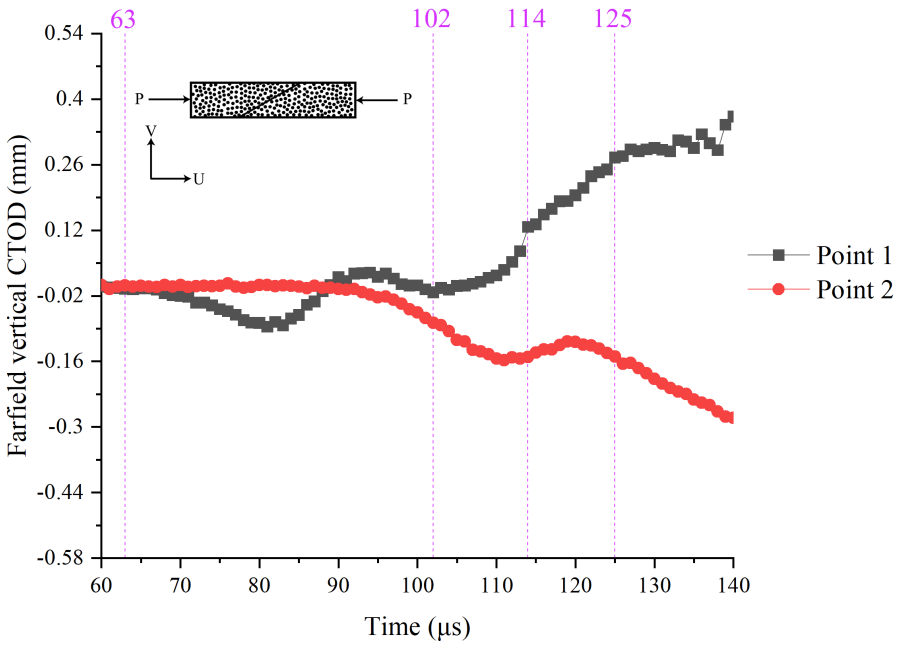

Figure 3.32: Vertical farfield results 2mm away from crack tip for test 5 showing stress wave transitions by vertical line

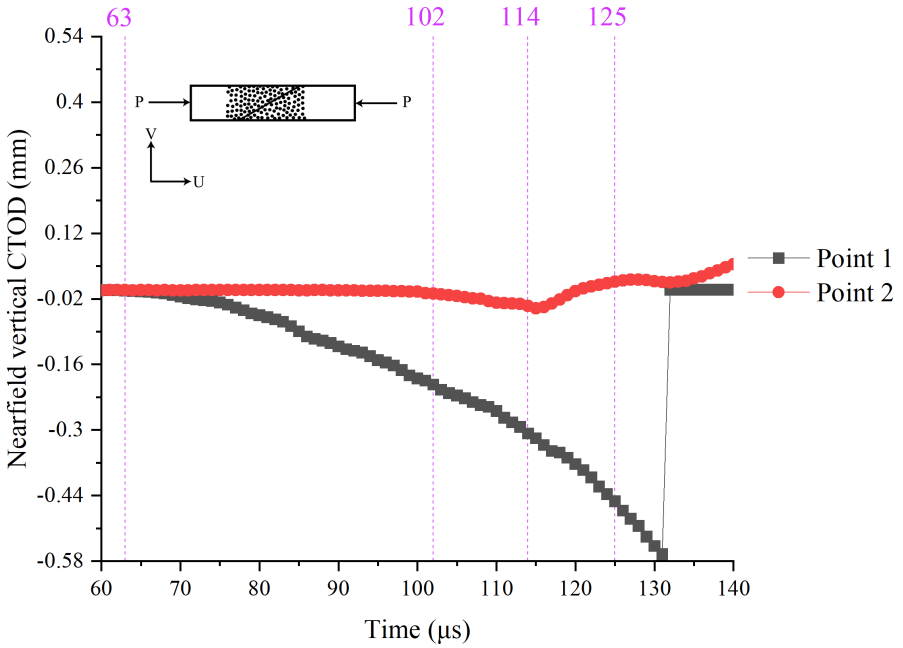

Figure 3.33: Vertical nearfield results 2mm away from crack tip for test 5 showing stress wave transitions by vertical line

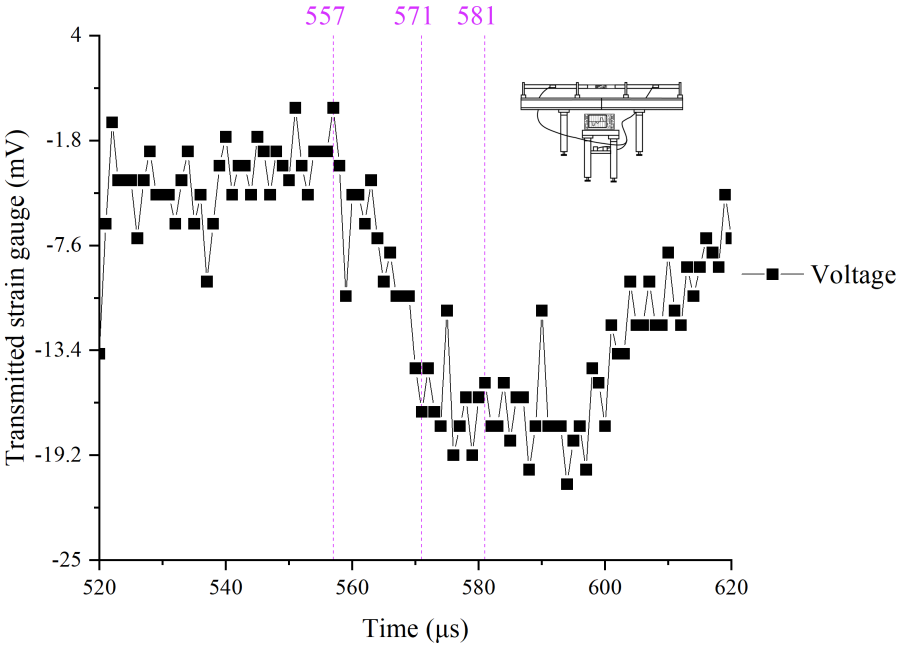

Figure 3.34: Split Hopkinson pressure bar raw values of test 6 with vertical lines indicating transfer of stress waves

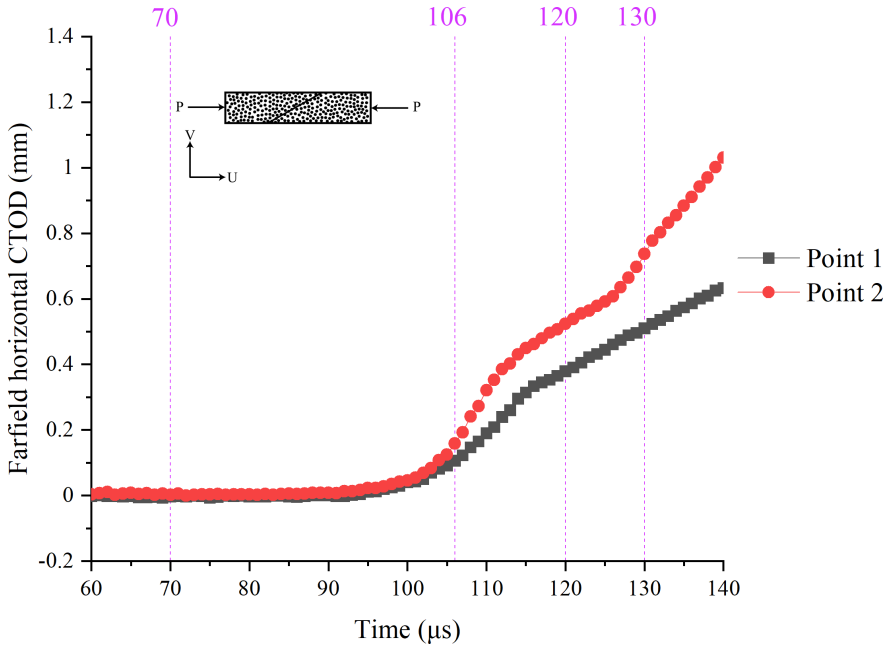

Figure 3.35: Horizontal farfield results 2mm away from crack tip for test 6 showing stress wave transitions by vertical line

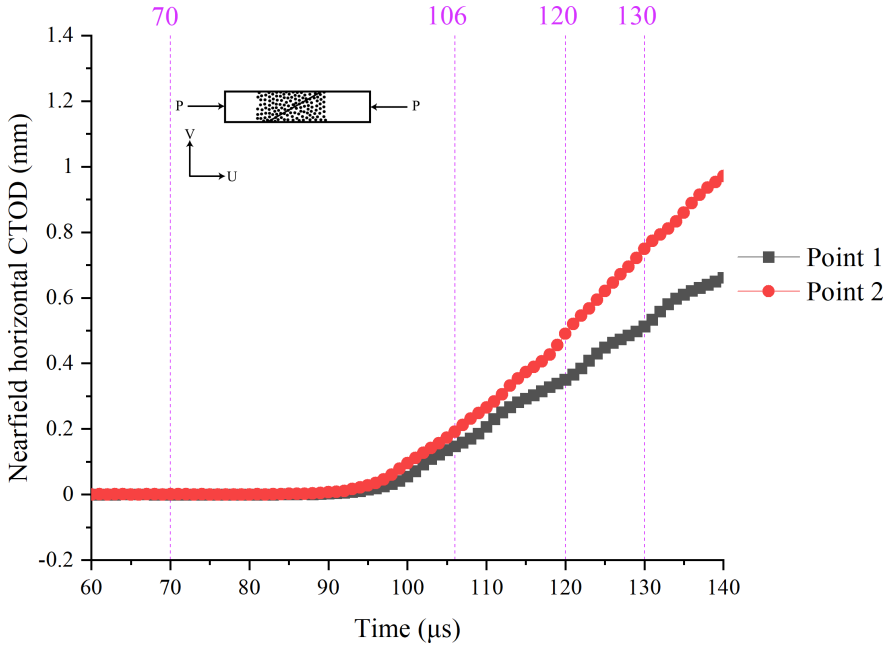

Figure 3.36: Horizontal nearfield results 2mm away from crack tip for test 6 showing stress wave transitions by vertical line

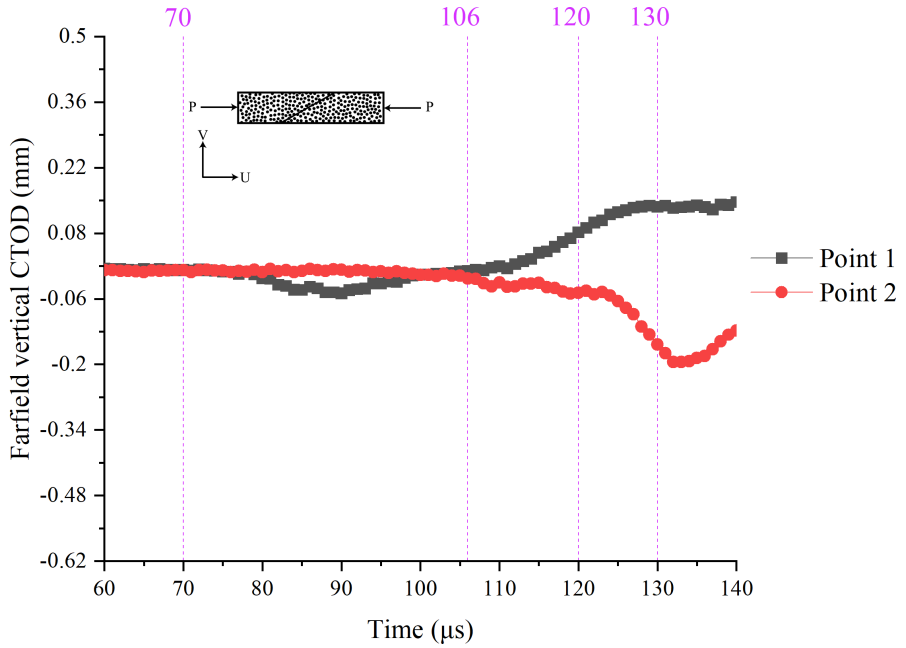

Figure 3.37: Vertical farfield results 2mm away from crack tip for test 6 showing stress wave transitions by vertical line

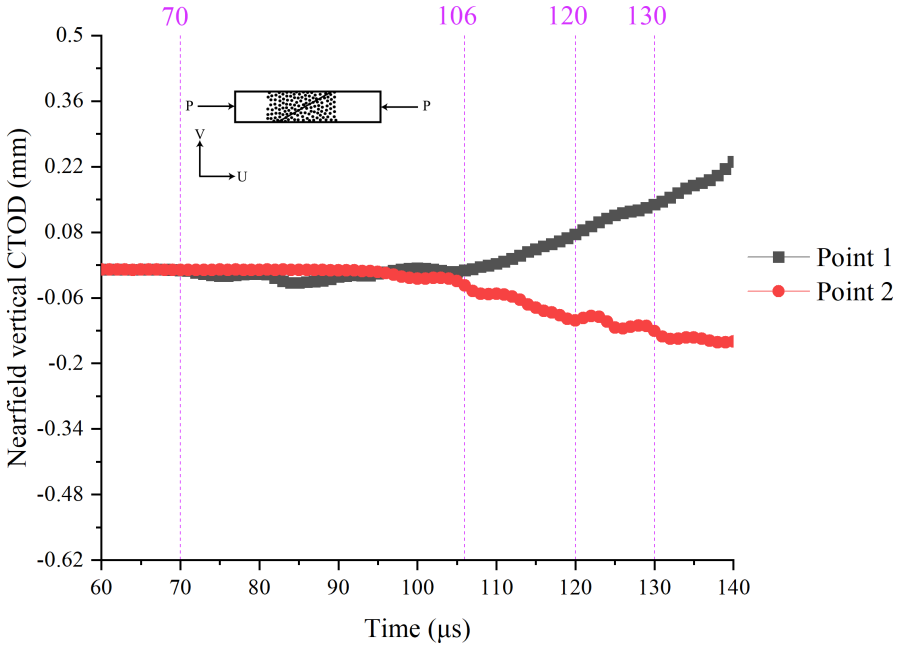

Figure 3.38: Vertical nearfield results 2mm away from crack tip for test 6 showing stress wave transitions by vertical line

Table 3.3: Polycarbonate along centrally cracked weakened planes dynamic fracture toughness for a weakened plane angle of 30°

Specimen #	**Fracture Mode**	**Farfield** $MPa\sqrt{m}$	**Nearfield** $MPa\sqrt{m}$	**SHPB** $MPa\sqrt{m}$
4	$\boldsymbol{K_{d,I}}$	1.33	1.23	1.34
	$\boldsymbol{K_{d,II}}$	0.68	0.53	0.78
	$\boldsymbol{K_{d,Mixed}}$	1.49	1.34	1.55
5	$\boldsymbol{K_{d,I}}$	1.33	1.48	1.47
	$\boldsymbol{K_{d,II}}$	0.68	0.59	0.85
	$\boldsymbol{K_{d,Mixed}}$	1.49	1.59	1.70
6	$\boldsymbol{K_{d,I}}$	1.29	1.35	1.34
	$\boldsymbol{K_{d,II}}$	0.49	0.43	0.78
	$\boldsymbol{K_{d,Mixed}}$	1.38	1.42	1.55

3.8 The 45 degree results

Three specimens were tested at 45 degree angles were completed, the results showed that there two equal modes of fracture in the mode I and II direction.

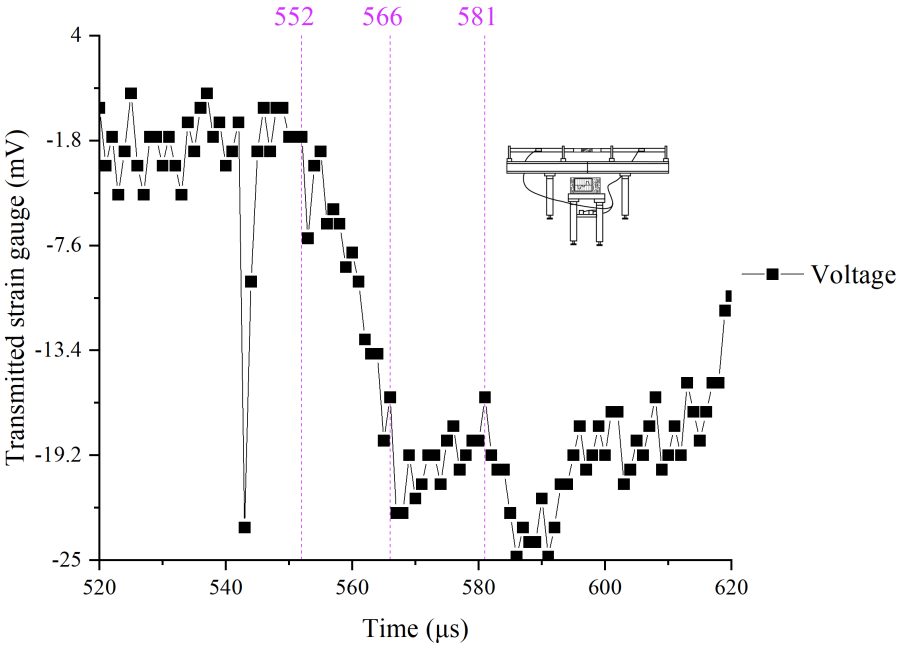

Figure 3.39: Split Hopkinson pressure bar raw values of test 7 with vertical lines indicating transfer of stress waves

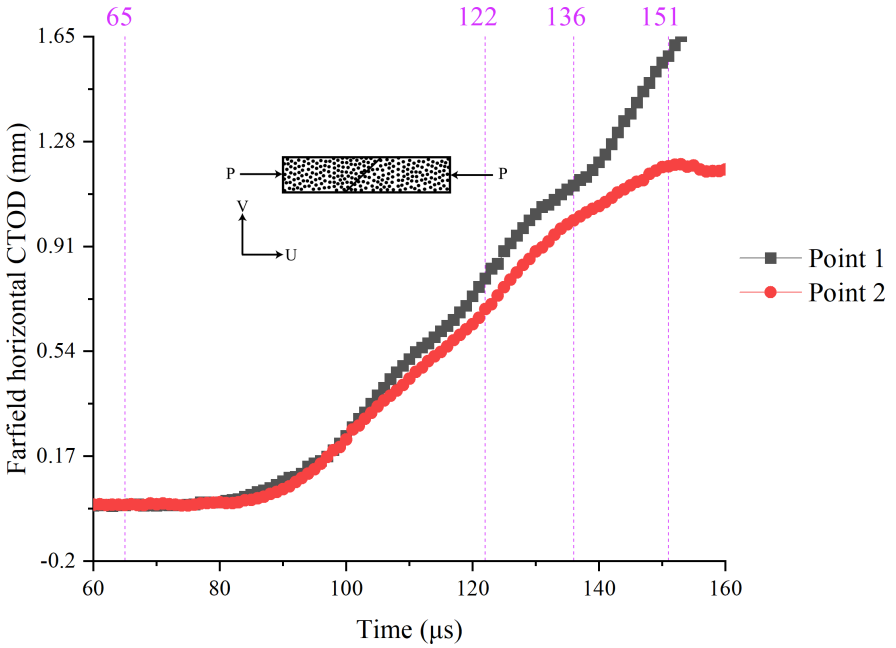

Figure 3.40: Horizontal farfield results 2mm away from crack tip for test 7 showing stress wave transitions by vertical line

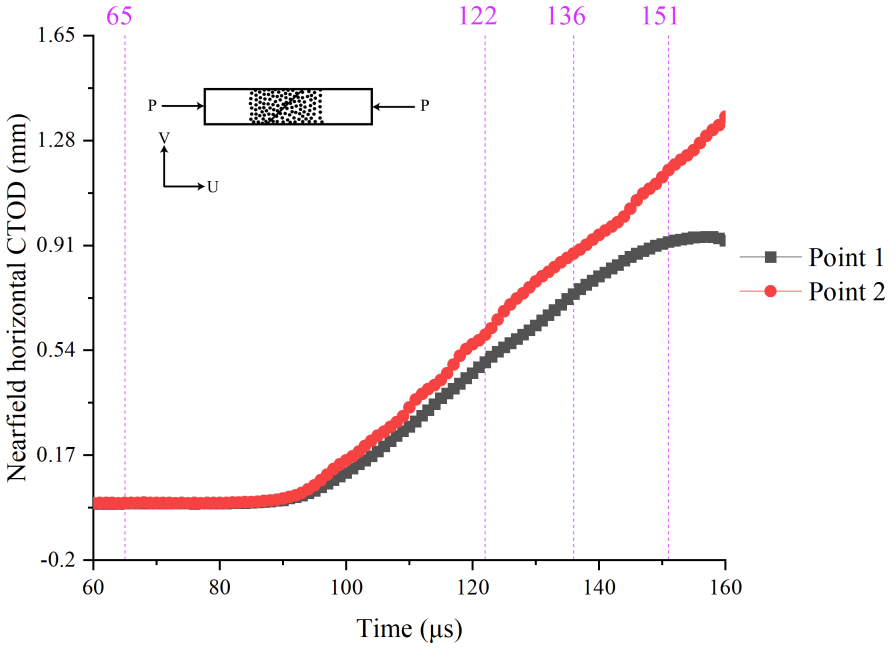

Figure 3.41: Horizontal nearfield results 2mm away from crack tip for test 7 showing stress wave transitions by vertical line

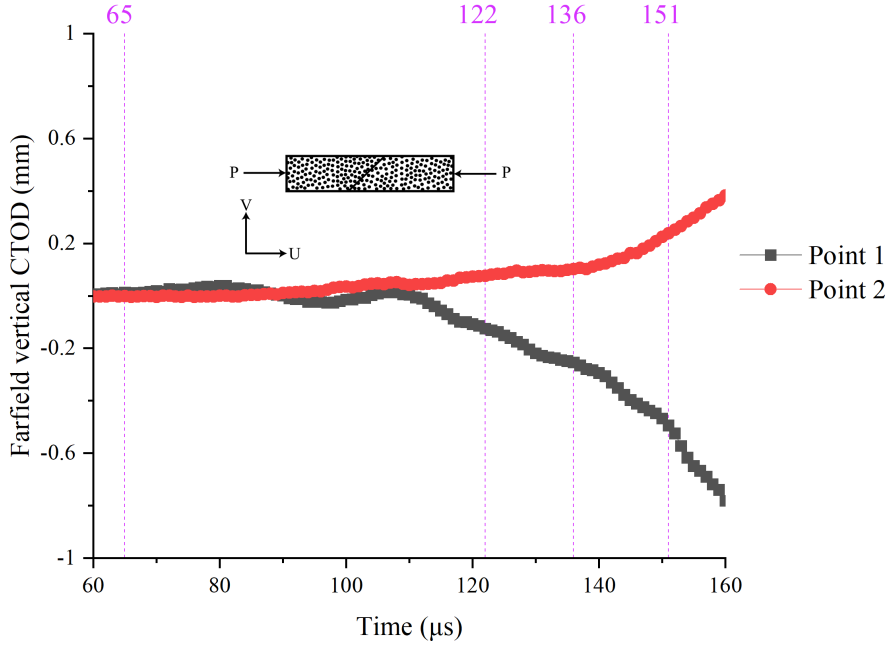

Figure 3.42: Vertical farfield results 2mm away from crack tip for test 7 showing stress wave transitions by vertical line

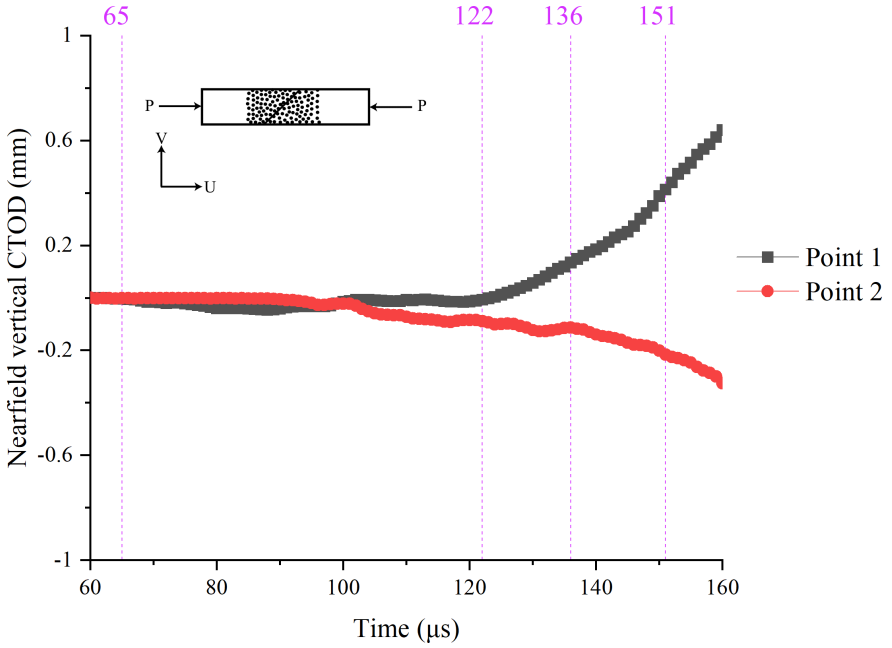

Figure 3.43: Vertical nearfield results 2mm away from crack tip for test 7 showing stress wave transitions by vertical line

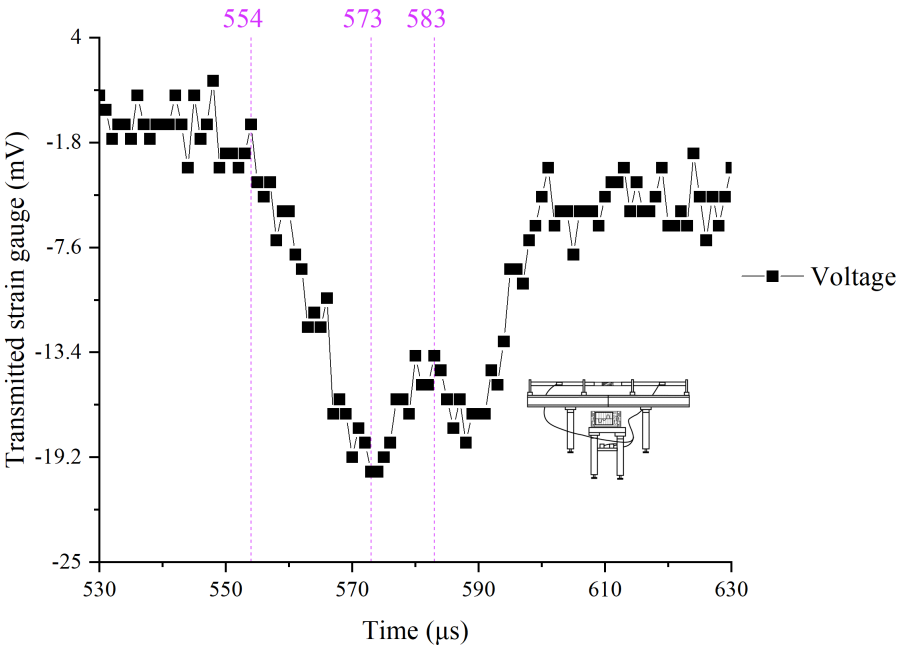

Figure 3.44: Split Hopkinson pressure bar raw values of test 8 with vertical lines indicating transfer of stress waves

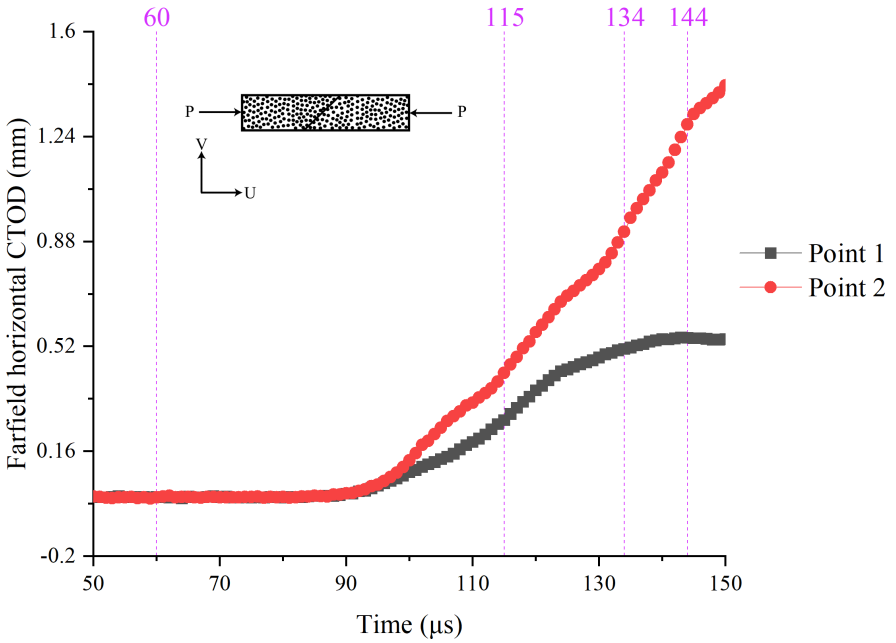

Figure 3.45: Horizontal farfield results 2mm away from crack tip for test 8 showing stress wave transitions by vertical line

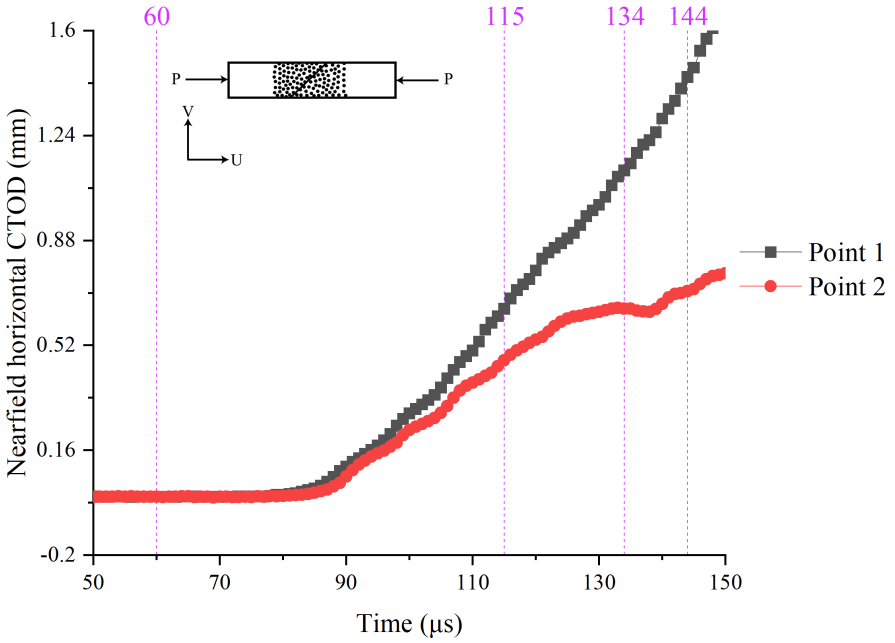

Figure 3.46: Horizontal nearfield results 2mm away from crack tip for test 8 showing stress wave transitions by vertical line

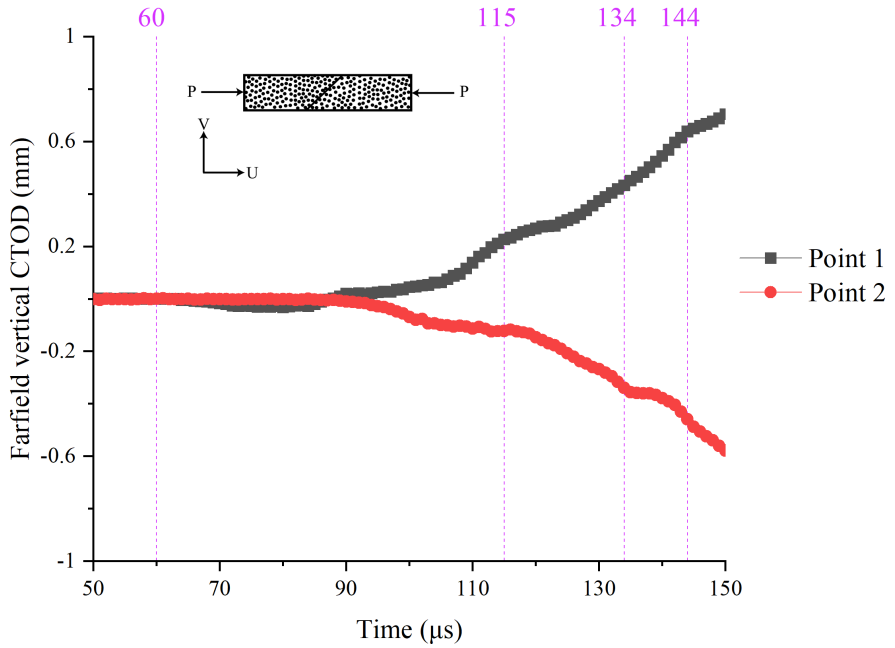

Figure 3.47: Vertical farfield results 2mm away from crack tip for test 8 showing stress wave transitions by vertical line

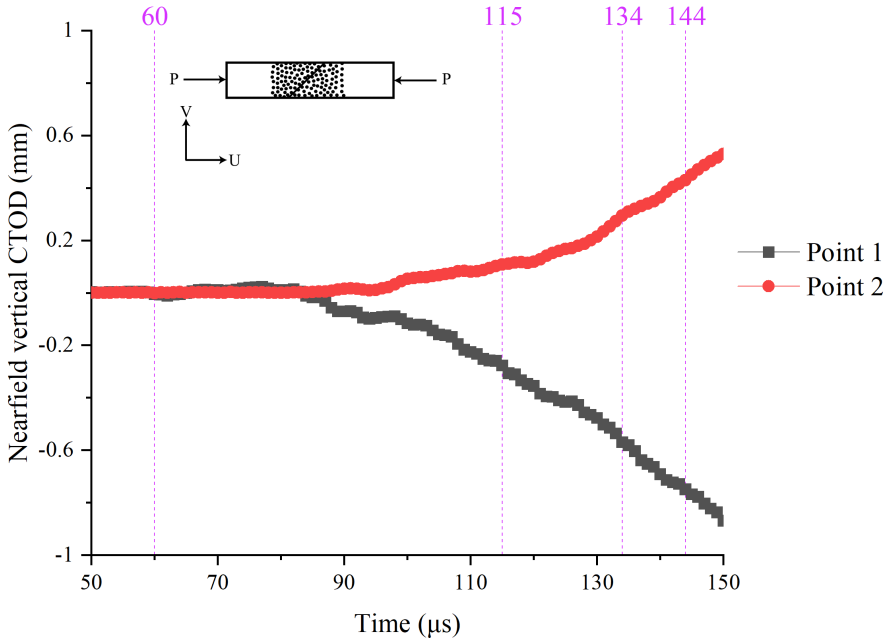

Figure 3.48: Vertical nearfield results 2mm away from crack tip for test 8 showing stress wave transitions by vertical line

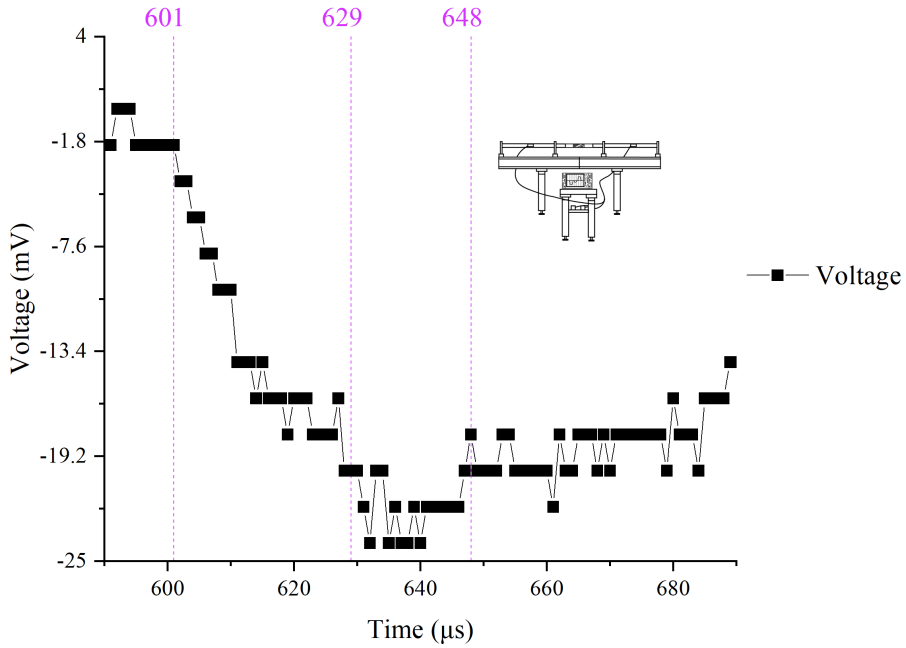

Figure 3.49: Split Hopkinson pressure bar raw values of test 9 with vertical lines indicating transfer of stress waves

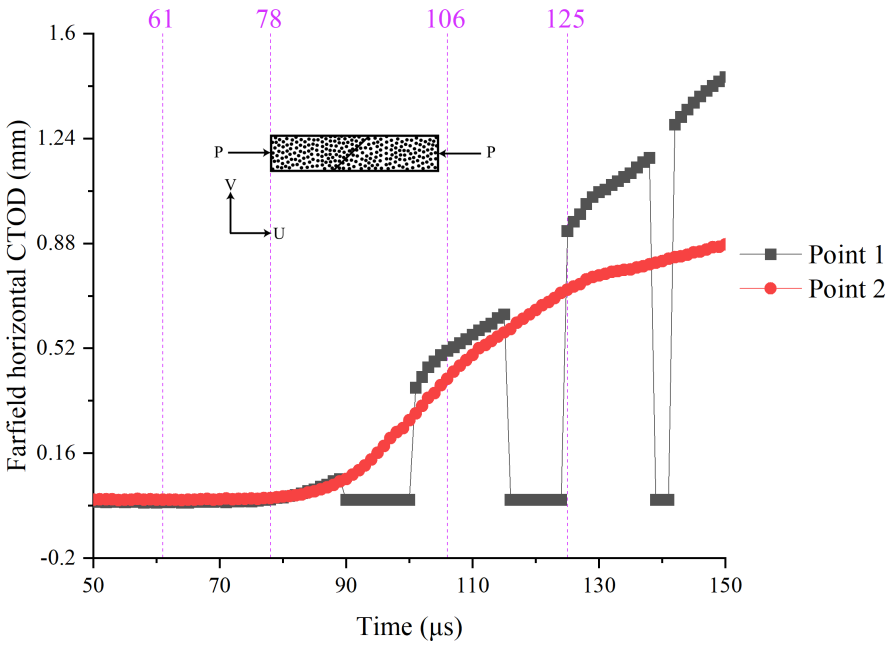

Figure 3.50: Horizontal farfield results 2mm away from crack tip for test 9 showing stress wave transitions by vertical line

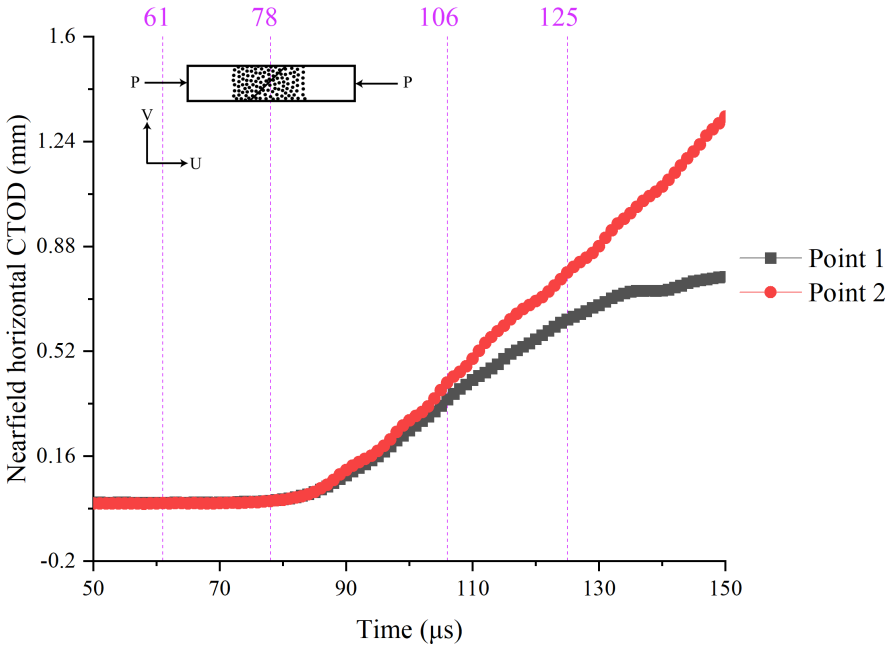

Figure 3.51: Horizontal nearfield results 2mm away from crack tip for test 9 showing stress wave transitions by vertical line

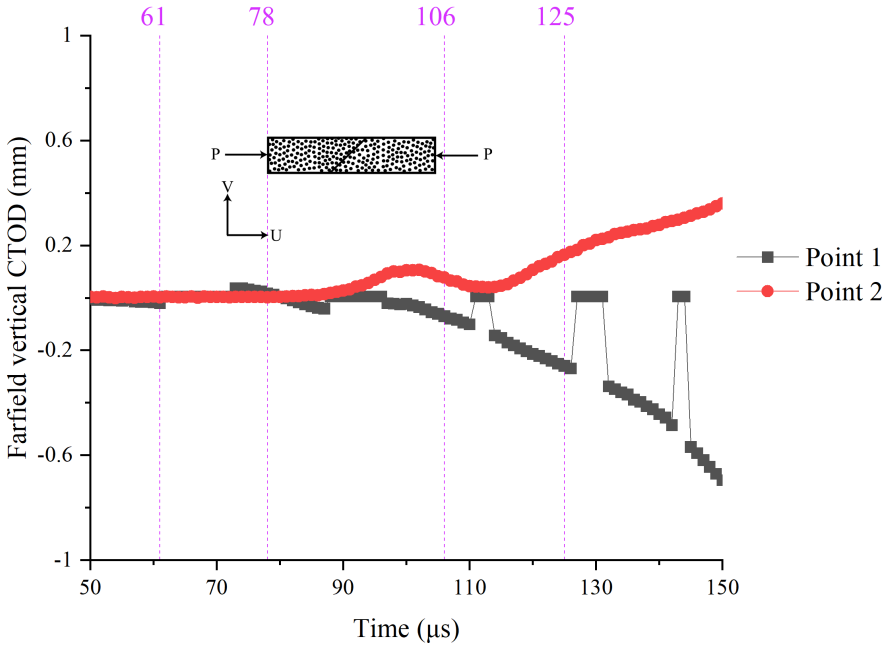

Figure 3.52: Vertical farfield results 2mm away from crack tip for test 9 showing stress wave transitions by vertical line

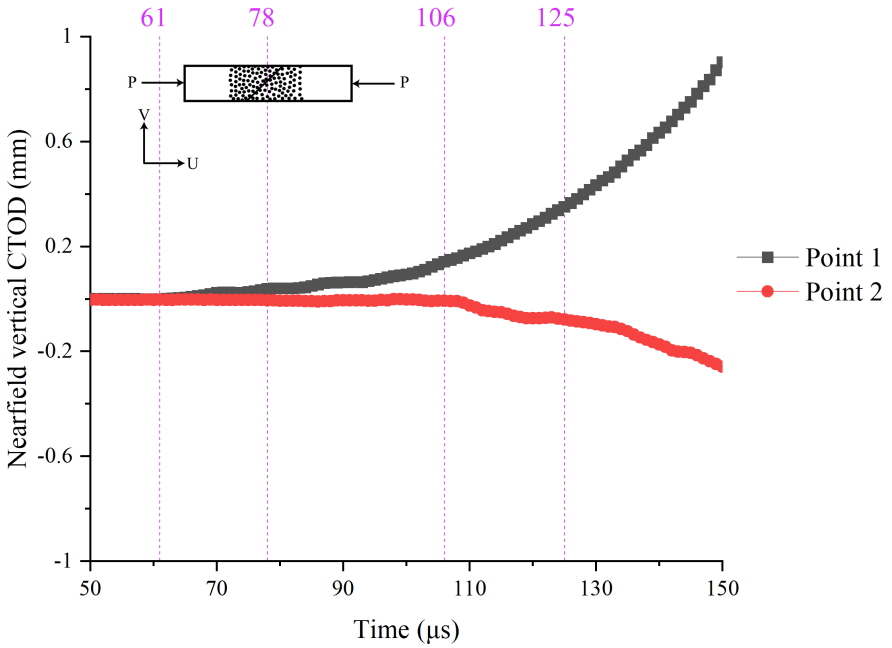

Figure 3.53: Vertical nearfield results 2mm away from crack tip for test 9 showing stress wave transitions by vertical line

Table 3.4: Polycarbonate along centrally cracked cyanoacrylate weakened planes dynamic fracture toughness for a weakened plane angle of 45°

Specimen #	**Fracture Mode**	**Farfield** $MPa\sqrt{m}$	**Nearfield** $MPa\sqrt{m}$	**SHPB** $MPa\sqrt{m}$
7	$\boldsymbol{K_{d,I}}$	0.78	0.69	0.94
	$\boldsymbol{K_{d,II}}$	0.69	0.65	0.94
	$\boldsymbol{K_{d,Mixed}}$	1.04	0.94	1.33
8	$\boldsymbol{K_{d,I}}$	0.88	1.02	0.80
	$\boldsymbol{K_{d,II}}$	0.71	0.85	0.80
	$\boldsymbol{K_{d,Mixed}}$	1.13	1.33	1.13
9	$\boldsymbol{K_{d,I}}$	0.94	0.75	1.06
	$\boldsymbol{K_{d,II}}$	0.89	0.73	1.06
	$\boldsymbol{K_{d,Mixed}}$	1.29	1.05	11.00

3.9 The 60 degree results

Three specimens were tested at 60 degree angles were completed, the results showed that the primary mode of failure Mode II and minor mode I failure.

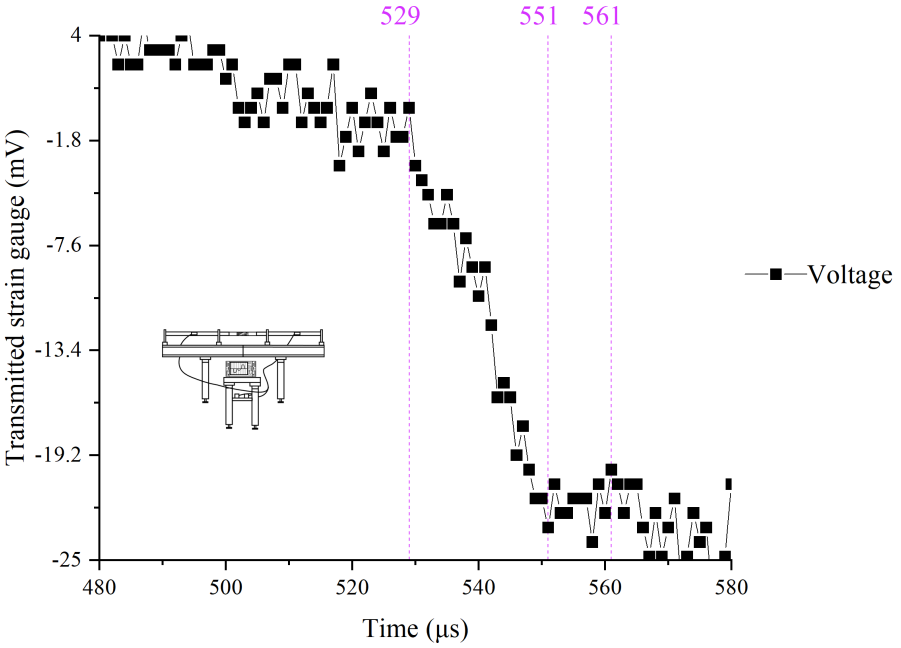

Figure 3.54: Split Hopkinson pressure bar raw values of test 10 with vertical lines indicating transfer of stress waves

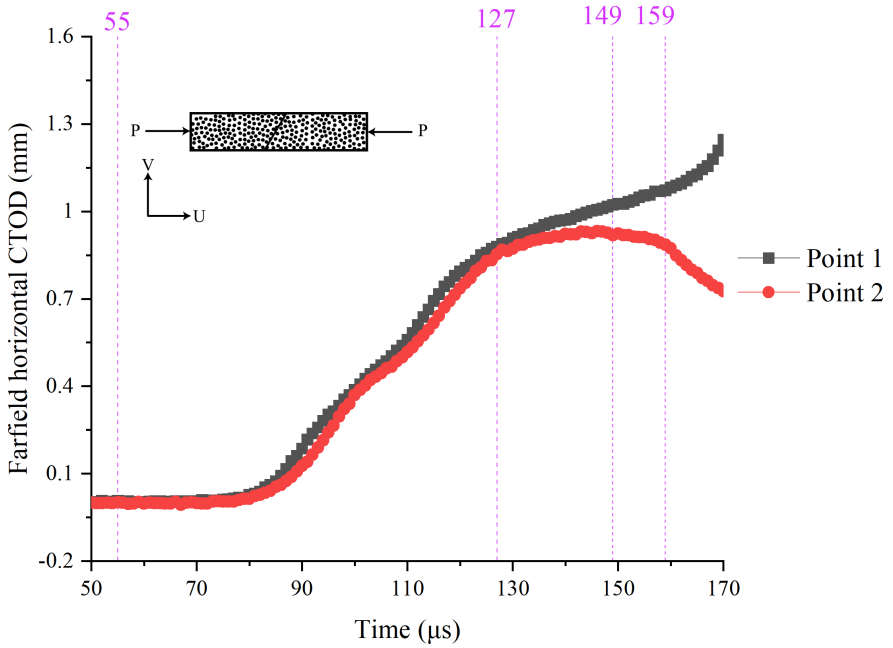

Figure 3.55: Horizontal farfield results 2mm away from crack tip for test 10 showing stress wave transitions by vertical line

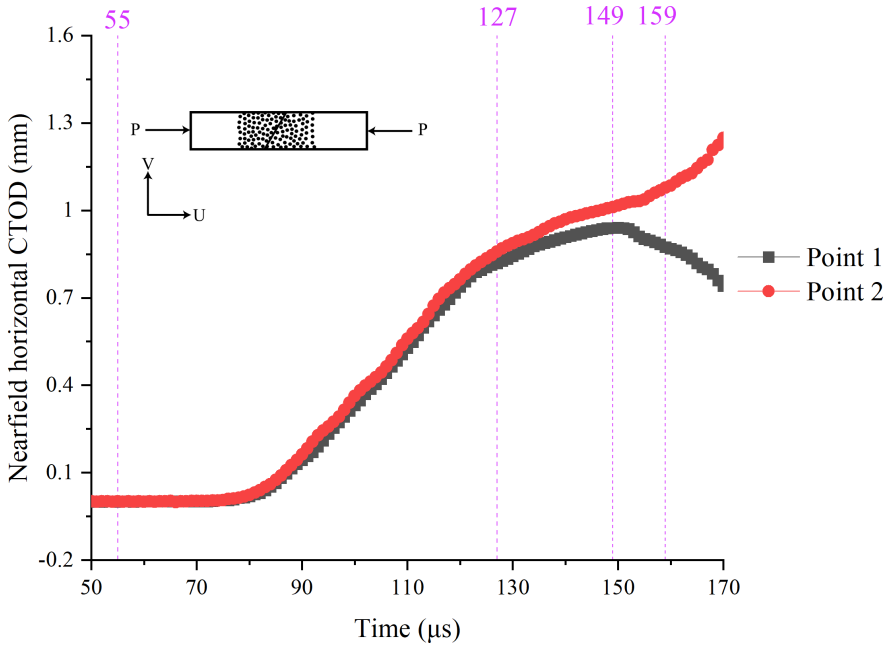

Figure 3.56: Horizontal nearfield results 2mm away from crack tip for test 10 showing stress wave transitions by vertical line

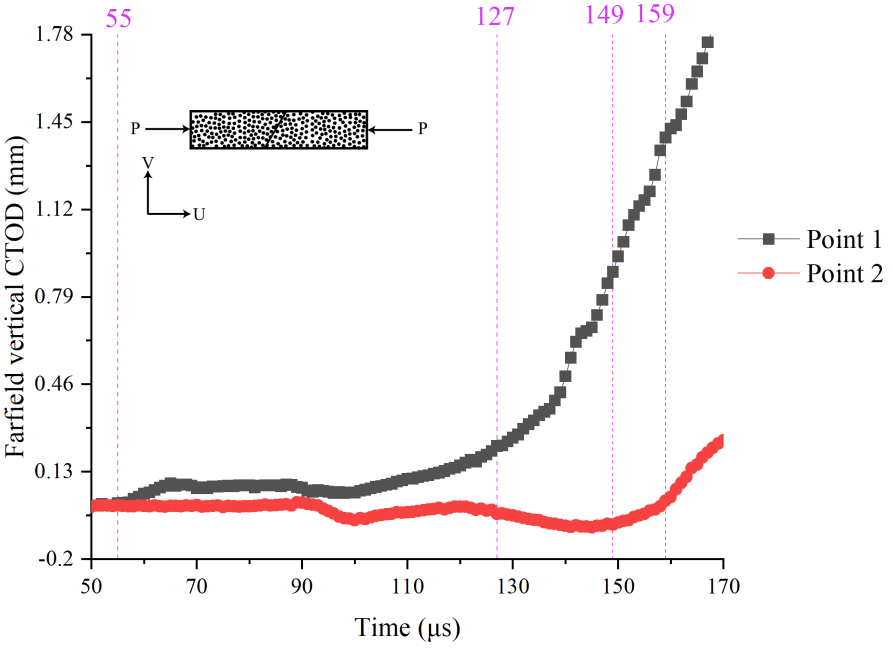

Figure 3.57: Vertical farfield results 2mm away from crack tip for test 10 showing stress wave transitions by vertical line

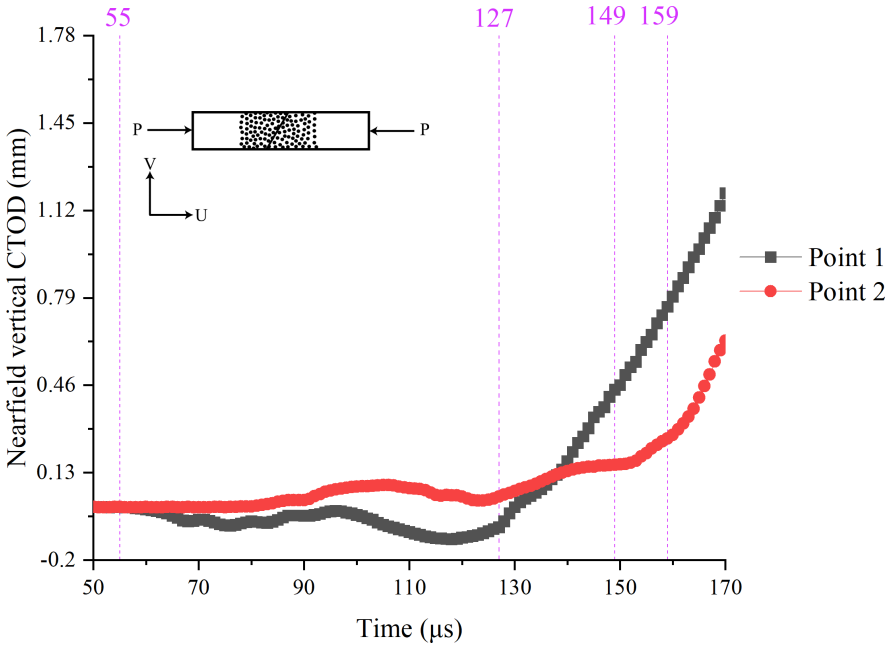

Figure 3.58: Vertical nearfield results 2mm away from crack tip for test 10 showing stress wave transitions by vertical line

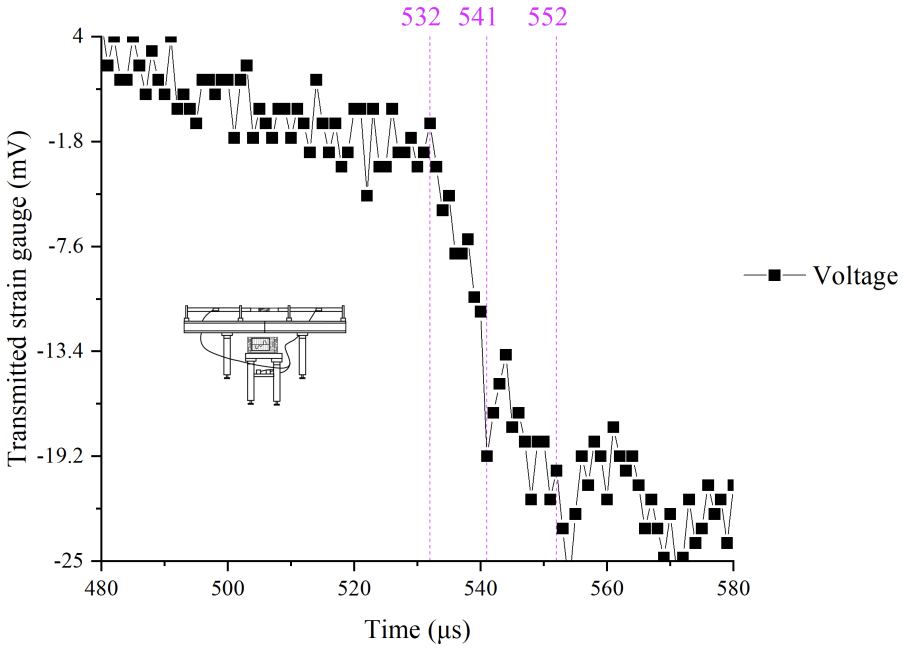

Figure 3.59: Split Hopkinson pressure bar raw values of test 11 with vertical lines indicating transfer of stress waves

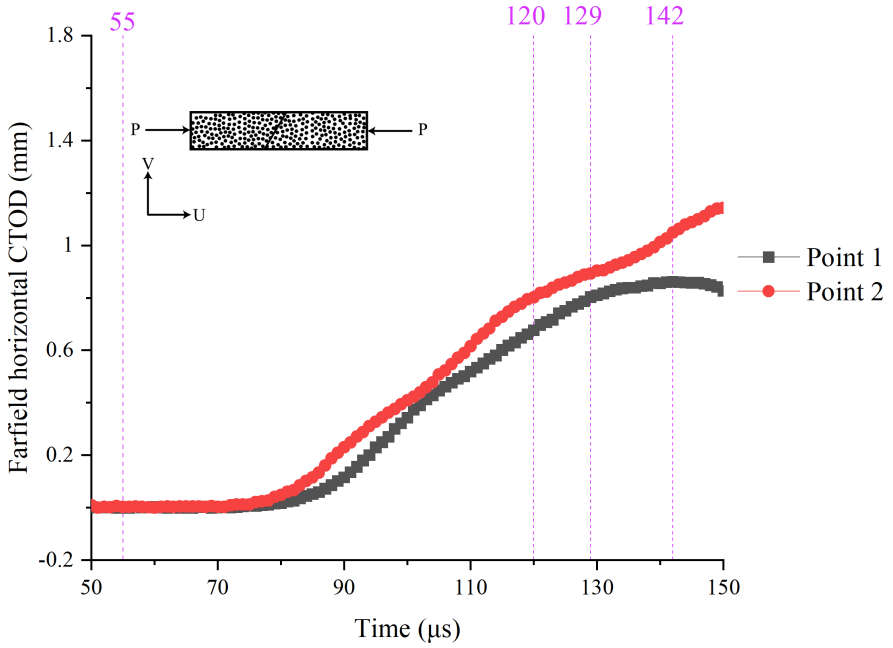

Figure 3.60: Horizontal farfield results 2mm away from crack tip for test 11 showing stress wave transitions by vertical line

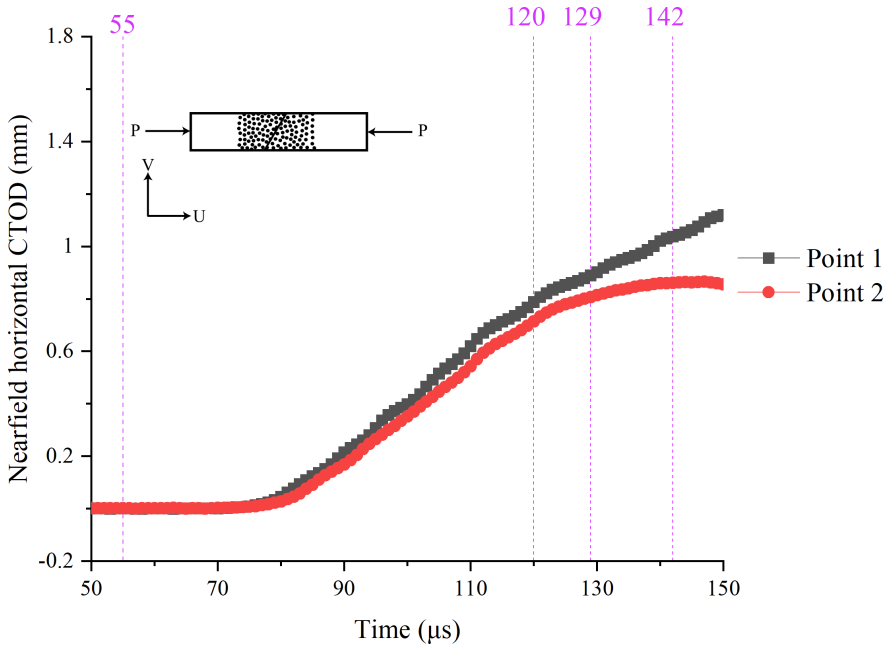

Figure 3.61: Horizontal nearfield results 2mm away from crack tip for test 11 showing stress wave transitions by vertical line

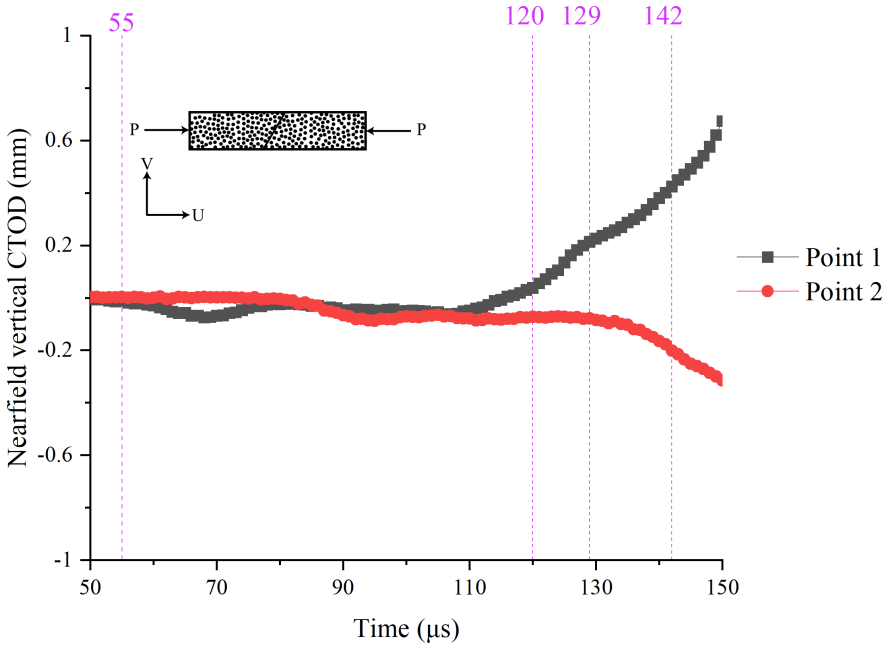

Figure 3.62: Vertical farfield results 2mm away from crack tip for test 11 showing stress wave transitions by vertical line

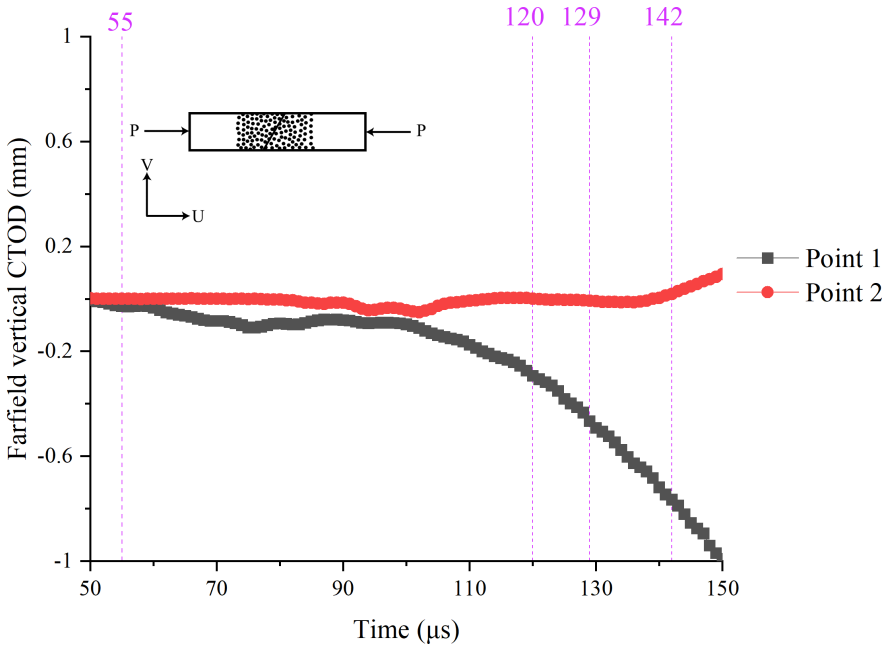

Figure 3.63: Vertical nearfield results 2mm away from crack tip for test 11 showing stress wave transitions by vertical line

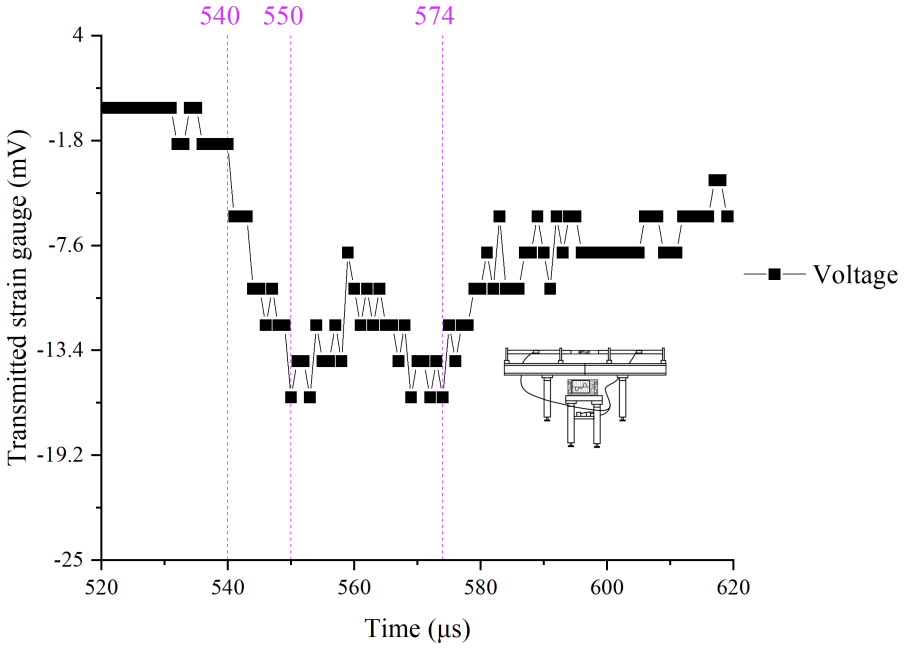

Figure 3.64: Split Hopkinson pressure bar raw values of test 12 with vertical lines indicating transfer of stress waves

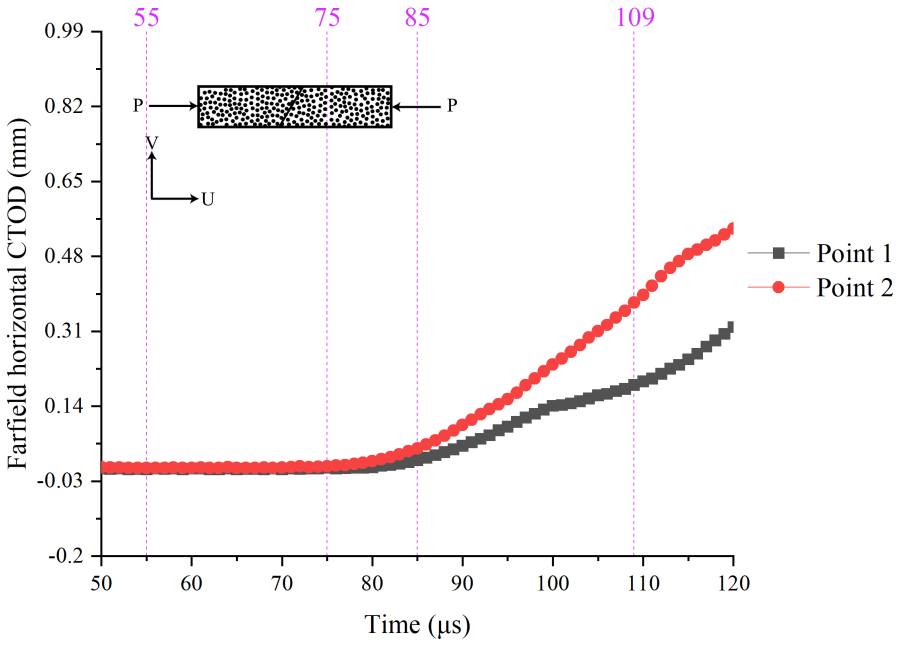

Figure 3.65: Horizontal farfield results 2mm away from crack tip for test 12

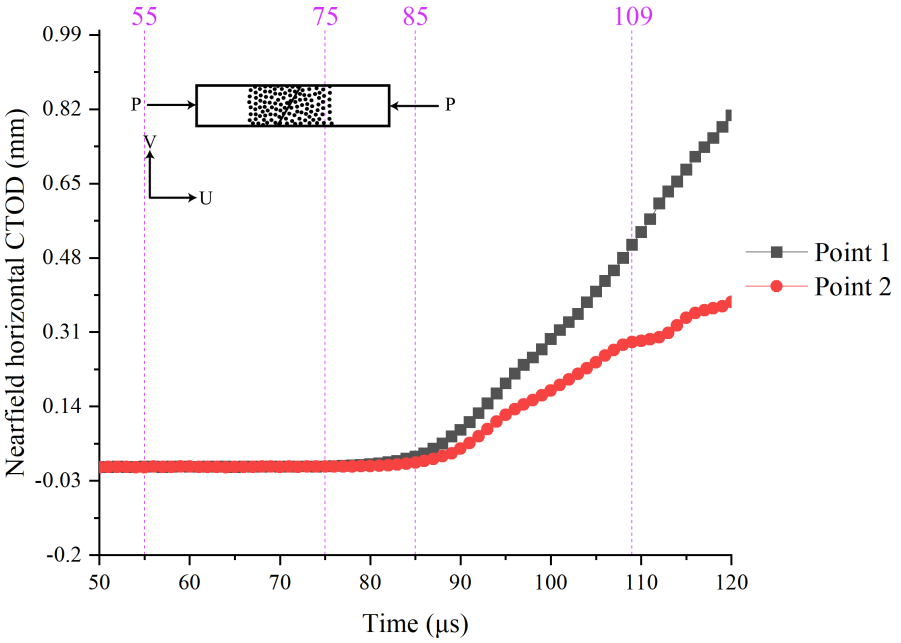

Figure 3.66: Horizontal nearfield results 2mm away from crack tip for test 12 showing stress wave transitions by vertical line

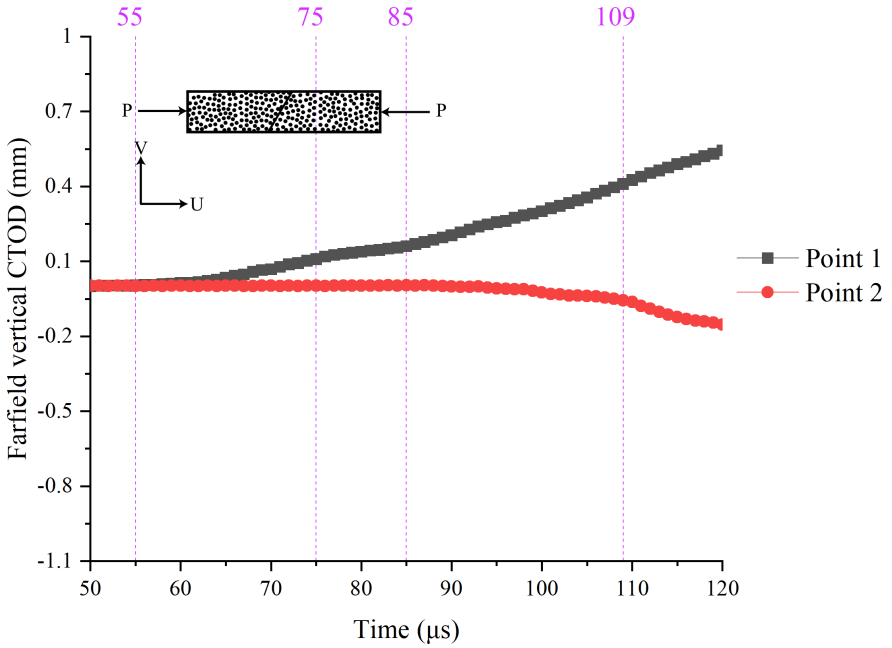

Figure 3.67: Vertical farfield results 2mm away from crack tip for test 12 showing stress wave transitions by vertical line

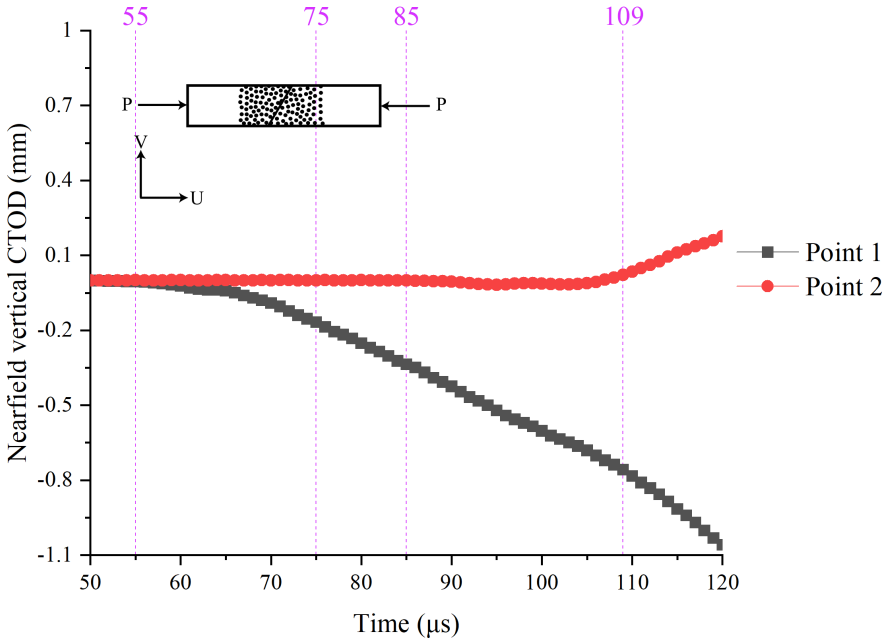

Figure 3.68: Vertical nearfield results 2mm away from crack tip for test 12 showing stress wave transitions by vertical line

Table 3.5: Polycarbonate along centrally cracked weakened planes dynamic fracture toughness for a weakened plane angle of 60°

Specimen #	**Fracture Mode**	**Farfield** $MPa\sqrt{m}$	**Nearfield** $MPa\sqrt{m}$	**SHPB** $MPa\sqrt{m}$
10	$\boldsymbol{K_{d,I}}$	0.61	0.67	0.66
	$\boldsymbol{K_{d,II}}$	1.66	1.57	1.14
	$\boldsymbol{K_{d,Mixed}}$	1.77	1.71	1.32
11	$\boldsymbol{K_{d,I}}$	0.76	0.93	0.76
	$\boldsymbol{K_{d,II}}$	1.51	1.35	1.51
	$\boldsymbol{K_{d,Mixed}}$	1.69	1.64	1.69
12	$\boldsymbol{K_{d,I}}$	0.62	0.74	0.53
	$\boldsymbol{K_{d,II}}$	1.12	1.68	1.83
	$\boldsymbol{K_{d,Mixed}}$	1.28	0.91	1.05

3.10 The 75 degree results

Three 75° tests were attempted and failed to achieved fracture on the specimen. Due to the 75° being able to transfer so much load without fracture, it is challenging to determine the fracture characteristics on the weakened planes if any at all. The extensive deformation can be explained by looking at the nature of the experimental apparatus and specimen configuration. The specimens weakened planes are very close to reaching the vertical and will not allow for sliding to take place without an extreme pressure wave not currently possible on the current experimental apparatus and if the pressure was possible, there is no guarantee that the specimen would fracture along the weakened plane. At such high pressures, the wave could fracture the bulk of the material along with the weakened planes. However, interpretations from the trend in Figure 3.69 show that the mode I fracture is dominate with little influences from mode II.

3.11 Fracture envelope and summary of results

Figure 3.69 depicts the fracture threshold values of centrally-cracked polycarbonate along weakened planes. The results indicates that fracture strength is dependent on the angle of the weakened plane and demonstrates that the least amount of load at the high strain rate is needed to cause fracture for a 45° weakened plane. As the weakened plane deviates from 45° to a lower angle, there is a considerable amount of loading needed to cause fracture in the mode II direction. On the contrary, mode I requires less loading to cause fracture. The opposite conditions is shown when the angle is higher than the 45° weakened plane. The loading needed to result in fracture is higher in the mode I direction. However, this results in a lower mode II loading capabilities. An important distinction about this fracture envelope is that the limiting fracture characteristic is the strength of the weakened plane, which in this case is cyanoacrylate adhesive.

The cyanoacrylate weakened planes on bulk polycarbonate fracture toughness average and standard deviation of three tests for all angles are summarized in table 3.6 showing an average value in addition to the standard deviation. These results are concurrent with expected values based on loading paths. The weakened planes govern the path of fracture and will slide across the weakened plane rather than fracture through the bulk of the specimen and this requires that the loading are based on sliding characteristics. There are cases when the fracture path or weakened plane angle becomes so high to the horizontal that the pressure wave will transfer through the bulk of the material as seen in the 75° angled specimens.

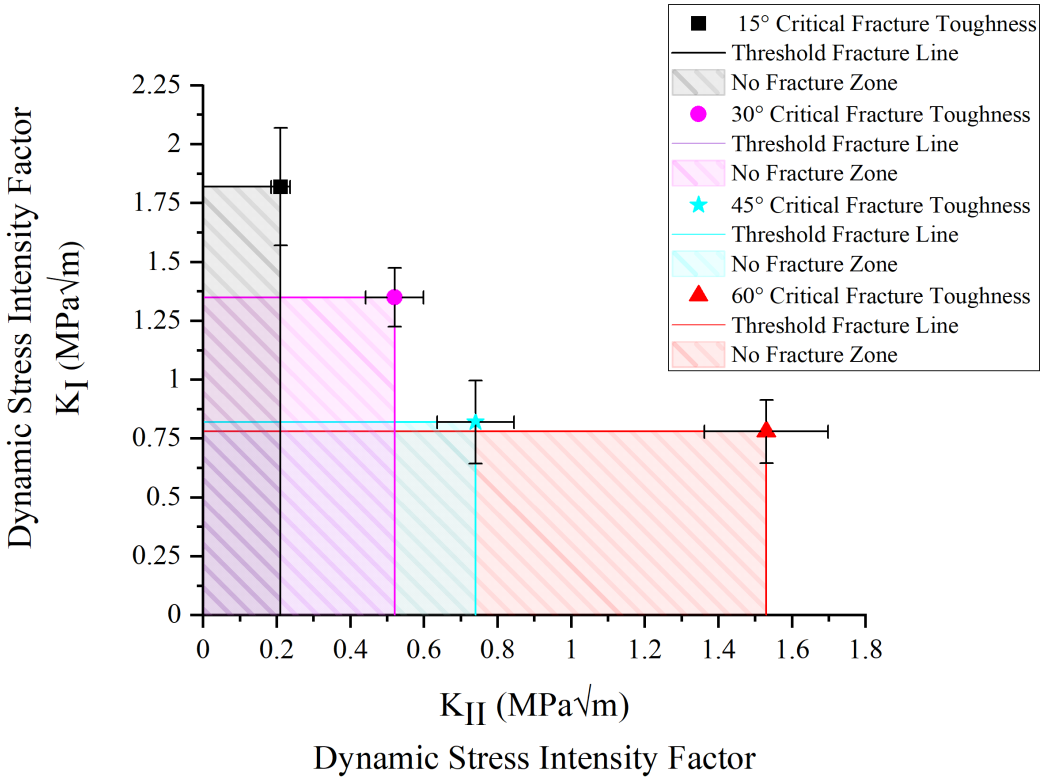

Figure 3.69: Fracture envelope showing angles of 15° 30°, 45° and 60° measured from the horizontal direction

Table 3.6: Cyanoacrylate weakened planes on bulk polycarbonate showing fracture toughness average and standard deviation of each angle for nearfield view

Angle °	**Fracture Mode**	**Average value and standard deviation** $MPa\sqrt{m}$
15	$K_{d,I}$	1.82 ± 0.25
	$K_{d,II}$	0.21 ± 0.03
	$K_{d,Mixed}$	1.83 ± 0.25
30	$K_{d,I}$	1.35 ± 0.13
	$K_{d,II}$	0.52 ± 0.08
	$K_{d,Mixed}$	1.45 ± 0.13
45	$K_{d,I}$	0.82 ± 0.18
	$K_{d,II}$	0.74 ± 0.10
	$K_{d,Mixed}$	1.11 ± 0.20
60	$K_{d,I}$	0.78 ± 0.13
	$K_{d,II}$	1.53 ± 0.17
	$K_{d,Mixed}$	1.73 ± 0.10

CHAPTER IV

Conclusion

Stress wave loading conditions were found to have significant effects on centrally cracked weakened planes on polycarbonate specimens by the use of three separate techniques; farfield, nearfield and SHPB. The stress waves would travel through the specimens and when the stress wave would interact with the weakened plane, the stress wave would cause the weakened plane interface to first elastically compress and second undergo shear compression until fracture of the weakened planes. The amount of loading at the high strain rates the specimen could withstand is based on the angle of the specimen.

The SHPB and DIC techniques have comparable fracture toughness values using LEFM. The weakened planes dictate the loading conditions and fracture path on the specimens. When the angle changed across the specimen's weakened plane, a relation will happen between the force transfer between mode I and mode II fracture characteristics. The mode of fracture to weakened plane angle relation is bulleted below:

- 15° results in $K_{d,II} >> K_{d,I}$
- 30° results in $K_{d,II} > K_{d,I}$
- 45° results in $K_{d,II} \approx K_{d,I}$
- 60° results in $K_{d,II} < K_{d,I}$

Weakened cyanoacrylate planes where tests at 15°, 30°, 45°, 60°, 75° to study the stress wave interactions across centrally cracked weakened planes. The results revealed that the stress wave interactions have a reaction to the

angle of the weakened planes. It was shown that low angles, based off the horizontal, 15° and 30° will result in a low shear fracture strength. To fracture a material with low angles, it is best to apply a stress in shear. However as the angle increases to high values such as 60° and 75°, the opposite is true. Fracture on high angles needs a stress in the tensile direction. When the angle is at 45° there is not a beneficial stress orientation to fracture the specimen. This is due to the 45° weakened plane's ability to uniformly share the stress in both shear and tensile orientations. It should be noted that the 75° weakened plane had the least effect on the fracture path due to the ability to transfer load to the bulk of the material and withstand copious amount of shear forces. This ability to transfer load at high strain rates prevents any stress concentration factors to build on the crack tip preventing failure.

CHAPTER V

Future work

The calculation of the J-integral and comparing to the methods discussed in this thesis. The advantage to using the J-integral is that it encompasses the plastic deformation and is a standard method to for non linear elastic fracture mechanics. The methods used in this thesis is based on LEFM. Ideally, the values from the J-integral should be comparable to the values shown in this thesis due to cyanoacrylate having brittle fracture characteristics.

References

Afolabi, A. O., Ojelabi, R. A., Omuh, I. O., and Tunji-Olayeni, P. F. (2019). 3D House Printing: A sustainable housing solution for Nigeria's housing needs. *Journal of Physics: Conference Series*, 1299(1):1–8.

Ameri, M., Mansourian, A., Heidary Khavas, M., Aliha, M., and Ayatollahi, M. (2011). Cracked asphalt pavement under traffic loading – a 3d finite element analysis. *Engineering Fracture Mechanics*, 78(8):1817–1826. Multi-axial Fracture.

Anderson, T. and Anderson, T. (2005). *Fracture Mechanics: Fundamentals and Applications, Third Edition*. Taylor & Francis.

Ayatollahi, M. and Aliha, M. (2009). Mixed mode fracture in soda lime glass analyzed by using the generalized mts criterion. *International Journal of Solids and Structures*, 46(2):311–321.

Barker, L. (1971). A model for stress wave propagation in composite materials. *Journal of Composite Materials*, 5(2):140–162.

Barouni, A. K. and Rekatsinas, C. S. (2021). Study on the propagation of stress waves in natural fiber composite strips. *Journal of Composites Science*, 5(1).

Bigun, J. (2006). *Vision with Direction: A Systematic Introduction to Image Processing and Computer Vision*. Springer Berlin Heidelberg.

Center for Photogrammetric Training (2020). HISTORY OF PHOTOGRAMMETRY. `https://ibis.geog.ubc.ca/courses/geob373/lectures/Handouts/History_of_Photogrammetry.pdf`. Online; accessed 15 September 2022.

Chu, T., Ranson, W., and Sutton, M. A. (1985). Applications of digital-image-correlation techniques to experimental mechanics. *Experimental mechanics*, 25(3):232–244.

Davies, R. M. and Taylor, G. I. (1948). A critical study of the hopkinson pressure bar. *Philosophical Transactions of the Royal Society of London. Series A, Mathematical and Physical Sciences*, 240(821):375–457.

Doyle, F. (1964). The historical development of analytical photogrammetry. *Photogrammetric Engineering*, 30(2):259–265.

Fahem, A. and Singh, R. (2021). Dynamic Damage Evolution in Shale in the Presence of Pre-existing Microcracks. *SEM Annual Conference, June 14-17, 2021*, 1(1):1–10.

Gruner, H. (1977). Photogrammetry: 1776-1976. *Photogrammetric Engineering and Remote Sensing*, 43(5):569–574.

He, L., Lin, F., Li, X., Sui, H., and Xu, Z. (2015). Interfacial sciences in unconventional petroleum production: from fundamentals to applications. *Chem. Soc. Rev.*, 44:5446–5494.

Hertz, H. (1882). Ueber die berührung fester elastischer körper.

Hopkinson, B. (1914). X. a method of measuring the pressure produced in the detonation of high, explosives or by the impact of bullets. *Philosophical Transactions of the Royal Society of London. Series A, Containing Papers of a Mathematical or Physical Character*, 213(497-508):437–456.

Hopkinson, J. and Hopkinson, B. (1901). *Scientific papers*. Original Papers by the Late John Hopkinson. At the University Press.

J J O'Connor and E F Robertson (2002). Siméon Denis Poisson. `https:`

//mathshistory.st-andrews.ac.uk/Biographies/Poisson/. Online; accessed 15 September 2022.

Jia, C., Zheng, M., and Zhang, Y. (2016). Some key issues on the unconventional petroleum systems. *Petroleum Research*, 1(2):113–122.

Keita, E., Bessaies-Bey, H., Zuo, W., Belin, P., and Roussel, N. (2019). Weak bond strength between successive layers in extrusion-based additive manufacturing: measurement and physical origin. *Cement and Concrete Research*, 123:105787.

Kolsky, H. (1949). An investigation of the mechanical properties of materials at very high rates of loading. *Proceedings of the Physical Society. Section B*, 62(11):676–700.

Komurlu, E., Cihangir, F., Kesimal, A., and Demir, S. (2016). Effect of adhesive type on the measurement of modulus of elasticity using electrical resistance strain gauges. *ARABIAN JOURNAL FOR SCIENCE AND ENGINEERING*, 41:433–441.

Konecny, G. (1985). The international society for photogrammetry and remote sensing-75 years old, or 75 years young. *Photogrammetric Engineering and Remote Sensing*, 51(7):919–933.

Krafft, J. M., Sullivan, A. M., Tipper, C. F., and Taylor, G. I. (1954). The effect of static and dynamic loading and temperature on the yield stress of iron and mild steel in compression. *Proceedings of the Royal Society of London. Series A. Mathematical and Physical Sciences*, 221(1144):114–127.

Lamb, H. (1917). On waves in an elastic plate. *Proceedings of the Royal Society of London. Series A, Containing Papers of a Mathematical and Physical Character*, 93(648):114–128.

Le, T., Austin, S., Lim, S., Buswell, R., Law, R., Gibb, A., and Thorpe, T. (2012a). Hardened properties of high-performance printing concrete. *Cement and Concrete Research*, 42(3):558–566.

Le, T. T., Austin, S. A., Lim, S., Buswell, R. A., Law, R., Gibb, A. G., and Thorpe, T. (2012b). Hardened properties of high-performance printing concrete. *Cement and Concrete Research*, 42(3):558–566.

Li, Z., Wang, L., and Ma, G. (2020). Mechanical improvement of continuous steel microcable reinforced geopolymer composites for 3d printing subjected to different loading conditions. *Composites Part B: Engineering*, 187:107796.

Lindholm, U. (1964). Some experiments with the split hopkinson pressure bar. *Journal of the Mechanics and Physics of Solids*, 12(5):317–335.

Lundergan, C. D. and Drumheller, D. S. (1971). Propagation of stress waves in a laminated plate composite. *Journal of Applied Physics*, 42(2):669–675.

Luo, Y., Xie, H. P., Ren, L., Zhang, R., Li, C. B., and Gao, C. (2018). Linear Elastic Fracture Mechanics Characterization of an Anisotropic Shale. *Scientific Reports*, 8(1):1–12.

Ma, F., Deng, X., Sutton, M. A., Newman, J. C., Miller, K., and McDowell, D. (1999). A ctod-based mixed-mode fracture criterion. *ASTM Special Technical Publication*, 1359:86–110.

Magic Lantern Society (2020). About Magic Lanterns. `www.magiclanternsociety.org/about-magic-lanterns/`. Online; accessed 15 September 2022.

Marien, M. (2006). *Photography: A Cultural History*. Laurence King.

Meier, T., Rybacki, E., Backers, T., and Dresen, G. (2015). Influence of Bedding Angle on Borehole Stability: A Laboratory Investigation of Transverse Isotropic Oil Shale. *Rock Mechanics and Rock Engineering*, 48(4):1535–1546.

Mohr, S. and Evans, G. (2011). Long term forecasting of natural gas production. *Energy Policy*, 39(9):5550–5560.

Peters, W. and Ranson, W. (1982). Digital imaging techniques in experimental stress analysis. *Optical engineering*, 21(3):427–431.

Peters, W., Ranson, W., Sutton, M., Chu, T., and Anderson, J. (1983). Application of digital correlation methods to rigid body mechanics. *Optical Engineering*, 22(6):738–742.

Robertson, G. (2005). *Food Packaging: Principles and Practice, Second Edition*. Food science and technology. Taylor & Francis.

Sanjayan, J. G. and Nematollahi, B. (2019). Chapter 1 - 3d concrete printing for construction applications. In Sanjayan, J. G., Nazari, A., and Nematollahi, B., editors, *3D Concrete Printing Technology*, pages 1–11. Butterworth-Heinemann.

Sanjayan, J. G., Nematollahi, B., Xia, M., and Marchment, T. (2018). Effect of surface moisture on inter-layer strength of 3d printed concrete. *Construction and Building Materials*, 172:468–475.

Selvadurai, A. (2013). *Partial Differential Equations in Mechanics 1: Fundamentals, Laplace's Equation, Diffusion Equation, Wave Equation*. Partial differential equations in mechanics. Springer Berlin Heidelberg.

Sun, C. and Jin, Z. (2011). *Fracture Mechanics*. Elsevier Science.

Sutton, M., Orteu, J., and Schreier, H. (2009). *Image Correlation for Shape,*

Motion and Deformation Measurements: Basic Concepts,Theory and Applications. Springer US.

Sutton, M. A., Wolters, W., Peters, W., Ranson, W., and McNeill, S. (1983). Determination of displacements using an improved digital correlation method. *Image and vision computing*, 1(3):133–139.

Tan, L., Ren, T., Yang, X., and He, X. (2018). A numerical simulation study on mechanical behaviour of coal with bedding planes under coupled static and dynamic load. *International Journal of Mining Science and Technology*, 28(5):791–797.

Tasdemirci, A., Hall, I. W., Gama, B. A., and Guden, M. (2004). Stress wave propagation effects in two- and three-layered composite materials. *Journal of Composite Materials*, 38(12):995–1009.

Tian, Q. and Huhns, M. N. (1986). Algorithms for subpixel registration. *Computer Vision, Graphics, and Image Processing*, 35(2):220–233.

United States Department of Labor (2019a). Changes in basic minimum wages in non-farm employment under State Law: Selected Years 1968 to 2021. `https://www.dol.gov/agencies/whd/state/minimum-wage/history`. Online; accessed 14 September 2022.

United States Department of Labor (2019b). FHFA HPI CALCULATOR. `https://www.dol.gov/agencies/whd/state/minimum-wage/history`. Online; accessed 14 September 2022.

U.S. Energy Information Administration (2022). Annual Energy Outlook. `https://www.eia.gov/outlooks/aeo/`. Online; accessed 15 September 2022.

U.S. Energy Information Administration, U.S. Department of Energy (2015). Technically recoverable shale oil and shale gas resources : United Kingdom. https://www.eia.gov/outlooks/aeo/. Online; accessed 15 September 2022.

APPENDIX A

Geometry Factor Deviation

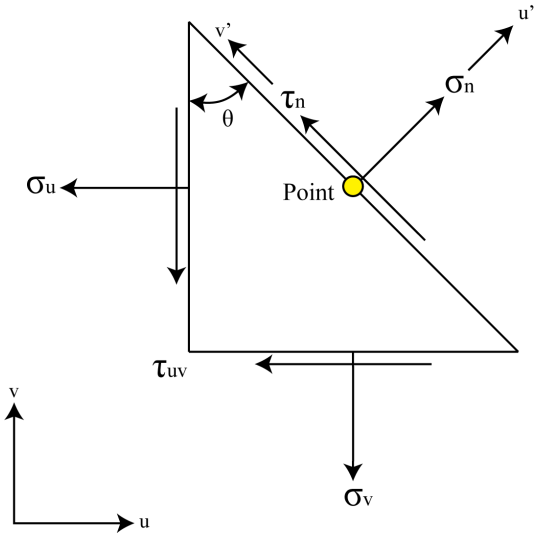

Figure A.1: Free body diagram on a triangular surface at an angle

Starting in the principal stress direction (mode I)

$\sum F_{u'} = 0$

$0 = \sigma_n dA - \sigma_u sin^2(\theta) - \sigma_v dA cos^2(\theta) - \tau_{uv} dA sin(\theta)cos(\theta) - \tau_{uv} dA sin(\theta)cos(\theta)$

The differential of the area cancels out

$0 = \sigma_n \cancel{dA} - \sigma_u \cancel{dA} sin^2(\theta) - \sigma_v \cancel{dA} cos^2(\theta) - \tau_{uv} \cancel{dA} sin(\theta)cos(\theta) - \tau_{uv} \cancel{dA} sin(\theta)cos(\theta)$

$0 = \sigma_n - \sigma_u sin^2(\theta) - \sigma_v cos^2(\theta) - \tau_{uv} cos(\theta)sin(\theta) - \tau_{uv} sin(\theta)cos(\theta)$

$\sigma_n = \sigma_u sin^2(\theta) + \sigma_v cos^2(\theta) + \tau_{uv} cos(\theta)sin(\theta) + \tau_{uv} cos(\theta)sin(\theta)$

The SHPB only applies stress in the horizontal direction; therefore $\sigma_v = 0$ and because this is uni-axial stress conditions $\tau_{uv} = 0$

$\sigma_n = \sigma_u sin^2(\theta) \quad \Rightarrow \quad \sigma_n = \sigma_u sin^2(\theta)$

This leaves a factor based on stresses and now completely dependent on geometry $\frac{\sigma_n}{\sigma_u} = sin^2(\theta)$

$$\boxed{Y = sin^2(\theta)}$$

Now looking at the principal shear direction (mode II)

$\sum F_{v'} = 0$

$0 = \tau_n dA - \sigma_u dA cos(\theta) sin(\theta) - \sigma_v dA sin(\theta) cos(\theta) - \tau_{uv} dA cos^2 + \tau_{uv} dA sin^2$

The differential of the area cancels out

$0 = \tau_n \cancel{dA} - \sigma_u \cancel{dA} cos(\theta) sin(\theta) - \sigma_v \cancel{dA} sin(\theta) cos(\theta) - \tau_{uv} \cancel{dA} cos^2 + \tau_{uv} \cancel{dA} sin^2$

$0 = \tau_n - \sigma_u cos(\theta) sin(\theta) - \sigma_v sin(\theta) cos(\theta) - \tau_{uv} cos^2 + \tau_{uv} sin^2$

$\tau_n = \sigma_u cos(\theta) sin(\theta) - \sigma_v sin(\theta) cos(\theta) - \tau_{uv} cos^2 + \tau_{uv} sin^2$

The SHPB onlv applies stress in the horizontal direction; therefore $\sigma_v = 0$ and because this is uni-axial stress conditions $\tau_{uv} = 0$

$\tau_n = \sigma_u cos(\theta) sin(\theta)$

This leaves a factor based on stresses and now completely dependent on geometry $\frac{\tau_n}{\sigma_u} = cos(\theta) sin(\theta)$

$\boxed{Y = cos(\theta) sin(\theta)}$

VITA

Kyle R. Messer

Candidate for the Degree of

Masters of Science

Thesis: DETERMINATION OF THE MIXED MODE STRESS INTENSITY FACTOR ON WEAKENED PLANES FOR CENTRALLY CRACKED POLYCARBONATE

Major Field: Materials Science and Engineering

Biographical:

Personal Data: Raised in Catoosa, OK.

Education: Completed the requirements for the degree of Masters of Science with a major in Materials Science and Engineering at Oklahoma State University in December, 2022.
Received a Bachelor of Science in Mechanical Engineering at the University of Tulsa in May 2019.